Analytical and Numerical Study of a Passive Self-Tuning Resonator

Majeed Altmizi

LUND
UNIVERSITY

Department of Mechanical Engineering

Division of Mechanics

Department of Mechanical Engineering
Division of Mechanics

ISRN LUTFD2/TFME – 18/5038 – SE(1-55)

Analytical and Numerical Study of a Passive Self-Tuning Resonator

Degree Project by
Majeed Altmizi

Supervisors:
Prof. Per Lidström, Division of Mechanics
Dr. Behrouz Afzali Far, MAX IV Laboratory

Printed by Media-Tryck, Lund, Sweden

For information address:
Division of Mechanics, Lund University, Box 118, SE-211 00 Lund, Sweden
Homepage: http://www.mek.lth.se

Preface

This thesis was carried out at the Division of Mechanics, Lund University. I thank Prof. Per Lidström for all his help and support, for his encouragement and dedication in me and this report. I also thank Dr. Behrouz Afzali Far for all his help and support. I also want to give a special thanks to my beloved family and mother, Halimeh Altmizi my biggest role model.

January, 2018

Majeed Altmizi

Abstract

Energy harvesting, from ambient vibrations, can be a very effective method for solving the problem with powering electronics were the need for constant power or regular battery replacements is a trouble or an inconvenience. But, since all energy harvesters, using mechanical vibrations, need to operate in resonance in order to generate maximal electrical output, and ambient vibrations usually do not have a constant vibration frequency, this results in the need for efficient self-tuning systems. This thesis presents an analytical study on the vibrational properties of passive self-tuning systems, based on the clamped-clamped beams and strings carrying a sliding mass. Numerical studies and modal analysis are presented and results are commented and explained. An attempt where made to reproduce the behavior of those systems in the commercial programs ADAMS and ABAQUS, the results and setbacks from those attempts are presented.

Keywords: Energy harvesting, mechanical vibrations, passive self-tuning, beam resonators, string resonators, sliding proof-mass, MEMS, actuators.

Contents

1 Introduction

1.1 Mechanical energy harvesting

The interest in energy harvesting has increased significantly over the last 20 years. The possibility to use the environment of a machine component in order to transform thermo-mechanical energy to electric energy has become a scientifically popular subject and numerous papers have been written about the subject, see for instance [1], [2].

There are various energy sources that could be harvested, such as light energy from ambient light, thermal energy from temperature gradients, volume flow of liquids or gases and mechanical energy from movements or vibrations. The use of mechanical energy harvesting could help powering wearables or small-scale electronics since the source for mechanical energy can be human movements or vibrations in structures.

The automatic spring device in a mechanical wrist watch is an example of a system harvesting energy from mechanical energy produced by human movements. In the mechanical wrist watch the wearers arm movement sets the weight in the watch in oscillation, enabling the automatic spring device to convert the transferred kinetic energy to potential energy in the main-spring, by way of the linked gear train [3].

In energy harvesting from mechanical vibrations the harvesting device needs to operate in resonance at the excitation frequency and this will limit the bandwidth at which they will work efficiently. Most vibration-based harvesters are designed as linear resonators with modified resonance frequencies to match the excitation frequencies for a specific application. In most applications, the ambient frequency is not constant and in return this will lead to a large loss of energy. There are ways to address this problem, either by using multiple systems or different tuning mechanisms. An ideal energy harvester is a system that can tune its resonance frequency with minimal or no energy consumption to match the ambient excitation frequency, [4], [5].

The resonance can be tuned using one of two methods; manual-tuning or self-tuning. Manual tuning is usually the easiest way since it mostly implicates changing the physical properties of the system, for example the spring stiffness or the structures center of mass, but it is very difficult to implement during operation. Self-tuning is expected to cover a targeted range of frequencies and to self-detect frequency change consuming as little harvested energy as possible, [2]. Furthermore, the self-tuning methods can be

implemented in two ways, the continuous and the intermittent. Continuous tuning, also referred to as active tuning, is defined as a tuning mechanism that is continuously active even when the resonance frequency of the device matches the excitation frequency, requiring continuous power input for tuning. Intermittent tuning, also referred to as passive tuning, is only using power during the tuning process and is passive when resonance is achieved, until the excitation frequency changes. There are various methods to implement the resonance tuning techniques and the methods can be categorized into mechanical, magnetic and electrical tuning.

In this thesis, the focus will be on energy harvesting from mechanical vibrations, more specifically on a passive self-tuning system.

1.2 Applications

Micro-electro-mechanical systems, commonly referred to as MEMS, [6], are micro-sized mechanical and electro-mechanical devices manufactured by using the techniques of micro-fabrication. Examples of components in MEMS are sensors, actuators, electronic and mechanical structures. The micro-sensors and micro-actuators are what make MEMS interesting. It is through these micro-components the MEMS get their functionality as devices that may convert energy from one form to another. The sensor typically converts a measured thermo-mechanical signal such as temperature, pressure, inertial forces, chemical species, magnetic fields and radiation to an electrical signal that can be sent to, or called for from, a monitoring device. The micro-actuators can be micro-valves for controlling liquid and gas flow, optical switches, micro-pumps or a variety of other actuators for different applications, [6]. While MEMS may solve a number of technical problems through their functionality and find a wide range of applications, a disadvantage is the power supply. MEMS are conventionally powered by chemical batteries. This leads to the problem with size limitations and the difficulties with replacing the batteries in sensors at hard to access places. Therefore energy harvesting, for MEMS and other sensors such as wireless sensor nodes (WSN), has become an important research topic during the last decade, [7].

Energy sources existing in the environment surrounding energy harvesting devices such as sunlight, wind, thermal gradients and mechanical vibrations are valuable assets for energy harvesting. Over the past few years a great amount of research has been made around energy harvesting of solar, thermo-electric and vibrational energy. There is a variety of products already on the

market using these harvesters, such as the solar charger, the thermoelectric wristwatch and wireless pushbutton switches. For MEMS and WSN energy harvesting from mechanical vibrations could be the most effective. Solar energy, even though being the most mature technology, is not cost effective. The solar cells need a large area for their disposal and they need to be clean. Furthermore, they only work where they can be reached by light. The limitations for thermal electric generators is the need for large thermal gradients and in a MEMS-compatible device it is hard to obtain overall gradients higher than 10°C, [8]

2 Background

2.1 Energy harvesting mechanisms

A vibration can come from a moving human body, air or water flow, a moving vehicle or any operating machine. The vibration can have various frequencies and amplitudes. Most devices for energy harvesting from mechanical vibrations are based on linear mass spring damper systems, also called linear energy harvesters.

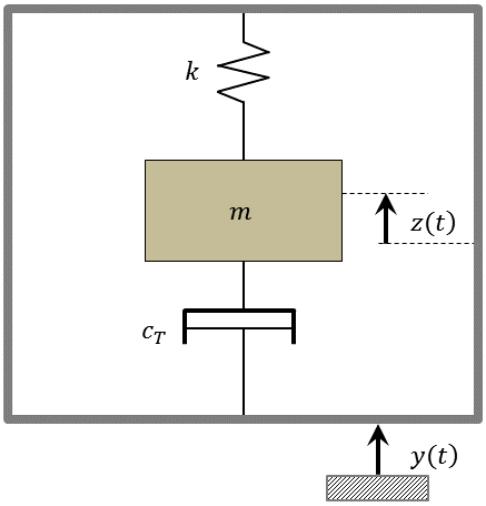

Figure 1. Schematic diagram of the linear, spring-mass-damping system.

Figure 1 above shows a linear spring-mass-damping system placed in a housing and consisting of an inertial mass, m, coupled to a spring with stiffness, k. The electrical energy harvested by the transducer and the energy lost through parasitic mechanisms is modelled as a linear viscous damper with

the damping coefficient, c_T, since the conversion from mechanical energy to electrical energy damps the motion of the mass. The housing is excited by an external sinusoidal vibration of the form $y(t) = Y\sin(\omega t)$. At resonance the housing will move out of phase with the inertial mass resulting in a net displacement, $z(t)$, between the mass and the housing [9],[10]. The differential equation describing the motion of the mass relative to the housing is given by

$$m\ddot{z}(t) + c_T\dot{z}(t) + kz(t) = -m\ddot{y}(t) \tag{1}$$

The transducer exploits either displacement or strain to extract electrical energy. There are three kinds of suitable transducers for energy harvesting of mechanical vibrations. These are the piezoelectric, the electromagnetic and the electrostatic transducers. Electrostatic and electromagnetic transducers use displacement while the piezoelectric transducers use strain to generate electrical energy.

If it is assumed that the vibration source is unaffected by the movement of the system, then the admitted power by the transducer and parasitic damping mechanism is given by, [9].

$$P(\omega) = \frac{m\zeta_T Y^2 \left(\frac{\omega}{\omega_r}\right)^3 \omega^3}{\left[1-\left(\frac{\omega}{\omega_r}\right)^2\right]^2 + \left[2\zeta_T \frac{\omega}{\omega_r}\right]^2} \tag{2}$$

where ζ_T is the relative damping, Y is the displacement amplitude of the housing and ω_r is the systems eigenfrequency. When the system operates in resonance the systems eigenfrequency matches the ambient vibration frequency and maximum power output will be achieved.

$$P = \frac{mY^2\omega_r^3}{4\zeta_T} \tag{3}$$

Eq. (2) is independent of which transducer is used. The greatest impact on the efficiency of the energy harvesting systems for mechanical vibrations is the ability of the system to match its eigenfrequency with the excitation frequency and reach resonance.

2.2 Self-tuning mechanisms

As mentioned, self-tuning can be achieved from one of two methods, active and passive self-tuning. Active self-tuning is a power consuming method since it is tuning the device using an externally supplied force or electrical signal to change the resonances of the energy harvester, by means such as controlling the stiffness or mass of the system. The need for external power makes the active self-tuning impractical for energy harvesting from mechanical vibrations. This since the power requirements often exceeds the energy possible to harvest from the available input vibrations that can be achieved for the intended applications. Therefore, passive self-tuning is of greater interest as the self-tuning method in energy harvesting from mechanical vibrations. This since in passive self-tuning there is no need for suppling any power to the tuning mechanism and the tuning itself only starts when the device is out of resonance.

There are specifically two passive self-tuning studies that caught our interest. In the first study Boudaoud et al., [11], conducted an experiment with a threaded bead on a clamped-clamped piano string shown in Figure 2. In [11] the vibration of the system was forced by an oscillating magnetic field generated by two U-shaped magnets and two iron plates.

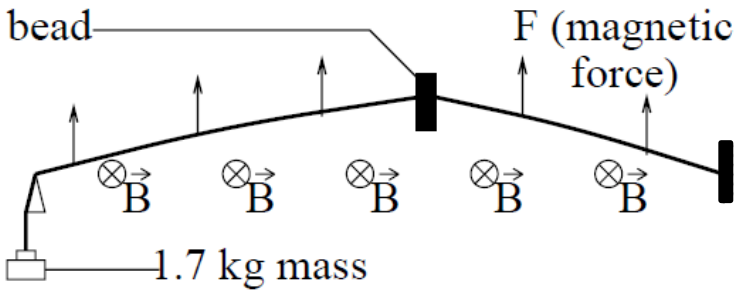

Figure 2. Schematic representation of the experimental apparatus presented in [11].

Boudaoud was able to demonstrate that when the string is forced to vibrate at a specific frequency, the bead would move to a position along the string so as to make the system resonant. Later on when the excitation frequency is changed the bead starts moving to a new position and once again sets the system in resonance. Boadaoud was thus able to show that a system with a clamped-clamped string with a sliding-bead adapts itself to become resonant when excited with a frequency from the systems frequency range through a slow dynamic process, [11].

In 2013 L.M. Miller published a paper, [12], on the experimental behavior of a self-tuning resonant system. The system is based on a beam resonator with a sliding proof-mass similar to the clamed-clamed string in Boadaoud's experiment.

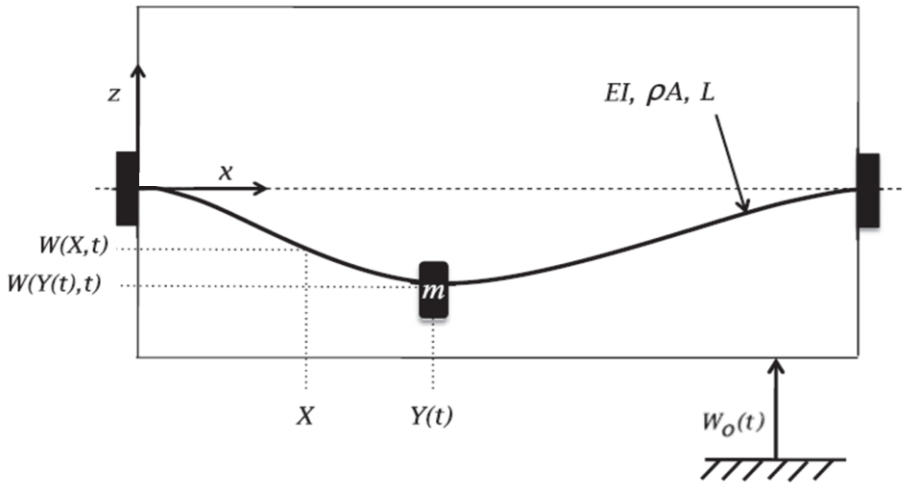

Figure 3. Schematic representation of the beam-mass resonator system presented in [12].

Figure 3 shows a clamped-clamped beam with sliding proof-mass and with the excitation displacement, $W_0(t)$. A point along the beam is identified by the coordinate, X, and the vertical displacement of the beam is defined by the function, $W = W(X,t)$. The horizontal position of the proof-mass is given by $Y = Y(t)$ and the vertical position of the proof-mass is given by, $W(Y(t),t)$. The experiment was conducted with a steel beam with the length 6 cm. As for the sliding proof-mass, a thermoplastic clamp is equipped with a small screw giving the proof-mass the desired weight. In Figure 3 it is possible to see how the deflection angels at the fixed points of the beam are lower than for the fixed point of the string, see Figure 2. Due to the difference in bending stiffness between the beam and string.

The experiments were conducted in two variants to verify two cases. In the first experiment, the proof-mass was placed at a chosen initial position and the system was subjected to a selected excitation frequency, in order to verify that the proof-mass would slide to the position on the beam that enables the system to achieve resonance.

As can be seen in Figure 4 the authors [12] were able to achieve the wanted behavior of the system. The motion of the proof-mass, is represented by the gray points (right vertical axis). It slides to the position on the beam that

enables the system to achieve resonance resulting in higher beam displacement amplitude represented by the black lines (left vertical axis). Passive self-tuning was observed at excitation frequencies of $80Hz$ and $140Hz$ at accelerations $\ddot{W}_0$ of $0.12g$ and $0.084g$, respectively.

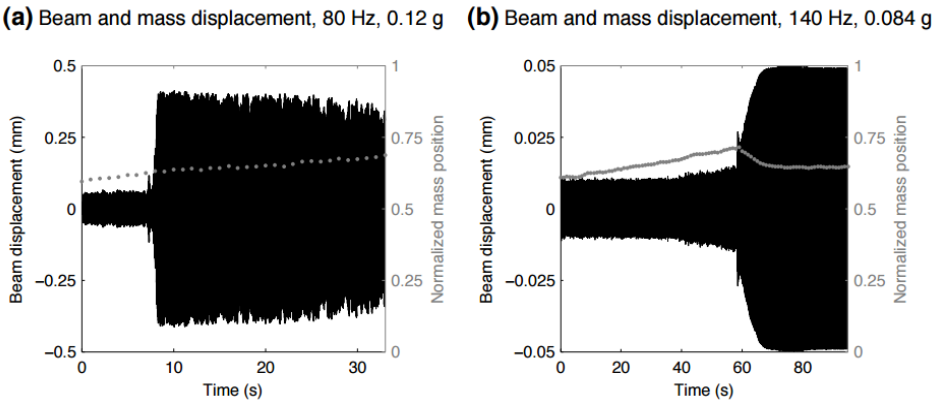

Figure 4. The passive self-tuning results from the experiment on a 6 cm steel beam mass system presented in L.M. Miller, P. Pillatsch, E. Halvorsen, P.K. Wright, E.M. Yeatman, A.S. Holmes, Experimental passive self-tuning behavior of a beam resonator with sliding proof -mass, J. Sound Vib. 332 (2013), [12]. Published with the consent of the author.

In the second experiment, the procedure from the first test was repeated but in this case, after the system reached resonance, the excitation frequency was changed in $1Hz$ increments over a given range. The purpose of these tests was to determine whether the proof-mass would slide to a new position that retuned the beam-mass systems resonance frequency to match the driving frequency and if it could stay tuned if the frequency was adjusted.

The experiment was successful and showed the wanted behavior. As can be seen in Figure 5 the proof-mass, represented as the gray points (right axis), continues to slide to new positions on the beam. During this process the system maintained the resonance resulting in the high displacement amplitude of the beam represented by the black lines (left axis). The resonance was successfully maintained as the frequency was adjusted up from $100Hz$ up to $140Hz$ by $1Hz$ increments and down from $100Hz$ to $70Hz$ by $1Hz$ decrements.

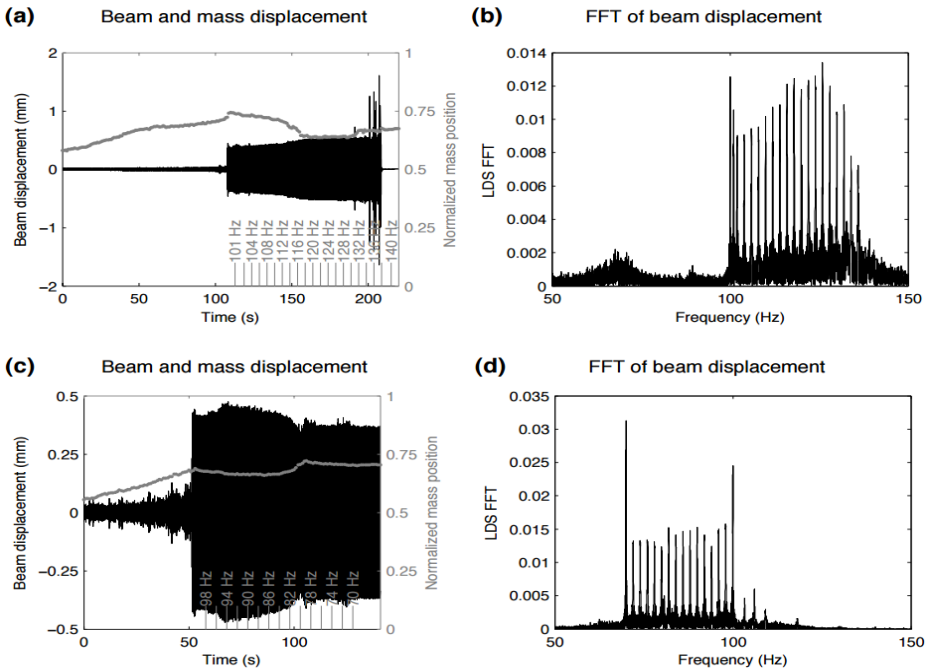

Figure 5. The results of maintaining passive self-tuning on a 6 cm beam mass system presented in L.M. Miller, P. Pillatsch, E. Halvorsen, P.K. Wright, E.M. Yeatman, A.S. Holmes, Experimental passive self-tuning behavior of a beam resonator with sliding proof-mass, J. Sound Vib. 332 (2013), [12]. Published with the consent of the author.

The result achieved by Miller et al., [12], shows that it is possible to use a beam resonator in passive self-tuning. It is also shown in the paper that the ability of the system to self-tune is not sensitive to the size or scale of the system.

The results from the experiments made by Boudaoud, [11], and Miller, [12], has been the inspiration for this thesis and for the following analytical work and an attempt to further understand the behavior of those systems, by deriving an analytical model, will be carried out in this thesis.

3 Self–tuning string and beam resonators

This part of the thesis is divided into four sections where, in section 3.1, the problem of the self-tuning string and beam resonators with a sliding proof-mass will be formulated. In section 3.2 the analytical work will be presented, starting with the formulation of the analytical model for the string resonators in 3.2.1. In 3.2.2 we proceed to present the analytical work for a beam resonator, presenting a solution for a beam with and without an axial preload.

Finishing section 3.2 with an application of the analytical model to the sliding proof-mass experiments by Miller [13]. In section 3.3, a numerical solution to the equations of motion for beam resonators is generated and calculations of the mode shapes are presented. In section 3.4, the simulation work done by using the softwares ADAMS and Abaqus, are presented and discussed.

3.1 Problem formulation

In the work done on beam resonators with sliding proof-mass, Miller [12], the behavior of the systems was studied through experimental procedures. It was observed that for a specific range of excitation frequencies the sliding-mass would move to the corresponding position of the beam that sets the system in resonance. This motivated the work on deriving an analytical model of the system in order to further investigate how different configurations of the system affect the frequency range and what effect the starting point of the sliding proof-mass has on the resonance behavior of the system. The system, consisting of the beam with sliding proof-mass, showed a high degree of complexity, especially in the interaction of the sliding proof-mass with the beam. Studying the work of Boudaoud [11] on string resonators with a sliding bead we could see that there are a lot of similarities with the behavior of the beam resonator with sliding proof-mass. Therefore, a study of a beam with axial preload is made in order to achieve a more string-like behavior of the beam.

The objective is to study and obtain more information of the behavior of the aforementioned resonator-systems and the behavior of their corresponding sliding-masses. Firstly, we present analytical models of the string and beam resonators. The equation of motion and the boundary conditions are formulated and the modal characteristic equation is derived in order to obtain the eigenfrequencies and the mode shapes. Later the computer aided simulation work of the systems will be presented.

3.2 Analytical study of the string and beam model

3.2.1 String model

The string model consists of a pre-tensioned string with a sliding proof-mass. The aim is to obtain the eigenfrequencies and the mode shapes of the system. In this model, the gravity is neglected. Figure 6 presents a general shape of the string and not a mode shape. The mode shapes are studied in Section 3.3.

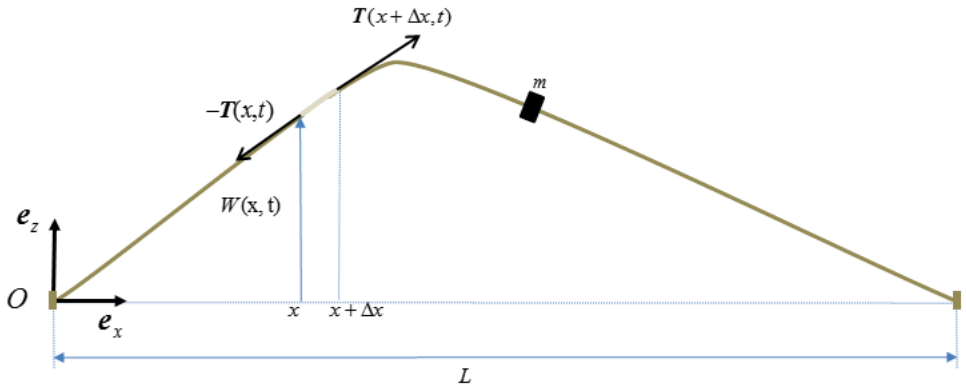

Figure 6. Schematic free body diagram of a string model.

A vibrating string with plane transverse string motion, with the displacement $W = W(x,t)$ and no external load will at time t have the following equation of motion [14].

$$\boldsymbol{T}(x+\Delta x,t) - \boldsymbol{T}(x,t) = m_s \Delta x \ddot{W}(x,t)\boldsymbol{e}_z \tag{4}$$

when letting $\Delta x \to 0$ we will get

$$\frac{\partial \boldsymbol{T}}{\partial x} = m_s \ddot{W}\boldsymbol{e}_z \tag{5}$$

where

$$\ddot{W} = \frac{\partial^2 W}{\partial t^2}(x,t) \tag{6}$$

$\boldsymbol{T} = \boldsymbol{T}(x,t) = T\boldsymbol{e}_t$ is the string traction vector with the tangential vector $\boldsymbol{e}_t = \boldsymbol{e}_t(x,t)$ and the string tension $T = T(x,t)$ and $m_s = \rho A(x)$ is the string mass per unit length with a constant density, ρ, and a cross-section area, $A = A(x)$.

The projection of Eq. (5) in the $\boldsymbol{e}_z$ direction, leads to

$$\boldsymbol{e}_z \cdot \frac{\partial \boldsymbol{T}}{\partial x} = m_s \ddot{W} \Rightarrow \frac{\partial}{\partial x}\left(\boldsymbol{e}_z \cdot \boldsymbol{T}\right) = m_s \ddot{W} \Rightarrow \frac{\partial}{\partial x}\left(\boldsymbol{e}_z \cdot \boldsymbol{e}_t T\right) = m_s \ddot{W} \tag{7}$$

Then, since

$$\boldsymbol{e}_t = \frac{\boldsymbol{e}_x + \boldsymbol{e}_z \dfrac{\partial W}{\partial x}}{\sqrt{1+\left(\dfrac{\partial W}{\partial x}\right)^2}} \tag{8}$$

Eq. (7) becomes

$$\frac{\partial}{\partial x}\left(\frac{\frac{\partial W}{\partial x}}{\sqrt{1+\left(\frac{\partial W}{\partial x}\right)^2}}T\right)=m_s\ddot{W} \tag{9}$$

It may be shown that $T(x,t)=\hat{T}(t)\sqrt{1+\left(\frac{\partial W(x,t)}{\partial x}\right)^2}$ and therefore Eq. (9) may be written

$$\frac{\partial^2 W}{\partial x^2}\hat{T}=m_s\ddot{W} \tag{10}$$

To solve the differential equation given in Eq.(10), the following harmonic solution is considered

$$W(x,t)=\hat{W}(x)\sin(\omega t) \tag{11}$$

Assuming that the pretension T as well as the mass per length $m_s(x)$ are constants ($\hat{T}(t)=T_0,\ m_s(x)=m_{s,0}$), the string equation is now given by

$$\frac{d^2\hat{W}}{dx^2}T_0\sin\omega t=-m_{s,0}\hat{W}\omega^2\sin\omega t \tag{12}$$

and can be rewritten as

$$\frac{d^2\hat{W}}{dx^2}+\Omega^2\hat{W}=0 \tag{13}$$

where

$$\Omega^2=\frac{\omega^2 m_{s,0}}{T_0} \tag{14}$$

To define the boundary conditions, the string is divided in two parts which are: [−] $0\le x\le s$ and [+] $s\le x\le L$. The parameter s denotes the position of the sliding-mass on the string see Figure 7. Consequently, the general solutions are given by

$$\begin{cases} \hat{W}^{-}(x) = a\sin(\Omega x) + b\cos(\Omega x), & 0 \le x \le s \\ \hat{W}^{+}(x) = c\sin(\Omega x) + d\cos(\Omega x), & s \le x \le L \end{cases} \tag{15}$$

where a, b, c, d are modal coefficients.

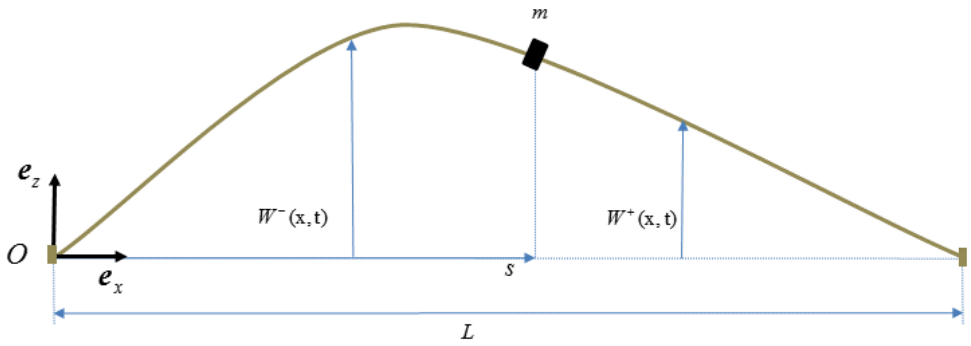

Figure 7. The two parts of the string model, (-) and (+).

To calculate the modal coefficients in Eq. (15), four boundary conditions are required. The first two boundary conditions are related to the fixed ends of the string as follows

$$\hat{W}^{-}(0) = 0, \ \hat{W}^{+}(L) = 0 \tag{16}$$

The third boundary condition is obtained where the sliding-mass is attached to the string. The displacements at the point $x = s$ for both parts of the sliding-mass are equal which is expressed by

$$\hat{W}^{-}(s) = \hat{W}^{+}(s) \tag{17}$$

Figure 8 shows the free body diagram of the sliding mass at the point, $x = s$. This gives us the following equation of motion

$$\boldsymbol{e}_t^{+}(s,t)T^{+} - \boldsymbol{e}_t^{-}(s,t)T^{-} = m\ddot{W}(s,t)\boldsymbol{e}_z \tag{18}$$

where m is the sliding-mass. By scalar multiplying Eq. (18) with $\boldsymbol{e}_z$ leads to

$$\frac{\dfrac{\partial W^{+}(s,t)}{\partial x}}{\sqrt{1+\left(\dfrac{\partial W^{+}(s,t)}{\partial x}\right)^2}}T^{+} - \frac{\dfrac{\partial W^{-}(s,t)}{\partial x}}{\sqrt{1+\left(\dfrac{\partial W^{-}(s,t)}{\partial x}\right)^2}}T^{-} = m\ddot{W}(s,t) \tag{19}$$

and assuming that $\left|\frac{\partial W^{+}(s,t)}{\partial x}\right| \ll 1$, $\left|\frac{\partial W^{-}(s,t)}{\partial x}\right| \ll 1$ gives us the approximate equation

$$\frac{\partial W^{+}(s,t)}{\partial x}T^{+} - \frac{\partial W^{-}(s,t)}{\partial x}T^{-} = m\ddot{W}(s,t) \tag{20}$$

which can be rewritten as

$$\frac{d\hat{W}^{+}(s)}{dx}T^{+} - \frac{d\hat{W}^{-}(s)}{dx}T^{-} = -\omega^{2}m\hat{W}(s) \tag{21}$$

By scalar multiplying Eq. (18) with $\boldsymbol{e}_x$ we get

$$\frac{1}{\sqrt{1+\left(\frac{\partial W^{+}(s,t)}{\partial x}\right)^{2}}}T^{+} - \frac{1}{\sqrt{1+\left(\frac{\partial W^{-}(s,t)}{\partial x}\right)^{2}}}T^{-} = 0 \tag{22}$$

Assuming that $\left|\frac{\partial W^{+}(s,t)}{\partial x}\right| \ll 1$, $\left|\frac{\partial W^{-}(s,t)}{\partial x}\right| \ll 1$ gives us the approximate equation

$$T^{+} - T^{-} = 0 \Rightarrow T^{+} = T^{-} = T_0 \tag{23}$$

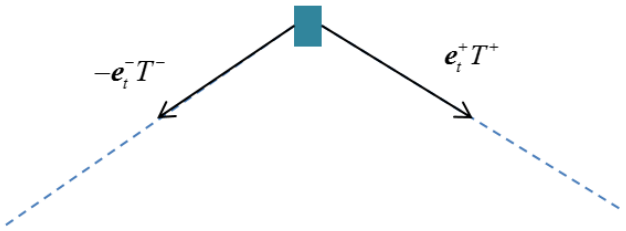

Figure 8. Free body diagram at point s.

Inserting the relation given in Eq. (23) in Eq.(21), leads to the fourth boundary condition.

$$\left(\frac{d\hat{W}^{+}}{dx} - \frac{d\hat{W}^{-}}{dx}\right)T_0 = -m\omega^{2}\hat{W} \tag{24}$$

Equation (15), along with the four boundary conditions given in Eqs. (16), (17) and (24), is used to set up a system of linear equations. Note that Eq. (16) implies that $b = 0$. Therefore, the system of equations is given by

$$\underbrace{\begin{pmatrix} 0 & \sin(\Omega L) & \cos(\Omega L) \\ \sin(\Omega s) & -\sin(\Omega s) & -\cos(\Omega s) \\ m\omega_n{}^2 \sin(\Omega s) - \Omega T_0 \cos(\Omega s) & \Omega T_0 \cos(\Omega s) & -\Omega T_0 \sin(\Omega s) \end{pmatrix}}_{=A} \begin{pmatrix} a \\ c \\ d \end{pmatrix} = \begin{pmatrix} 0 \\ 0 \\ 0 \end{pmatrix} \tag{25}$$

Finally, the eigenfrequency of the whole system, including the string and the sliding proof-mass, will be obtained by calculating the determinant of the $3\text{x}3$ -matrix given in Eq. (25) and solving the characteristic equation.

$$\det A = 0 \tag{26}$$

3.2.2 Beam model

In this thesis, the static and dynamic behavior of the beam is based on the Euler-Bernoulli theory, with the following assumptions:

- The material of the beam is isotropic.
- The material behavior is linear elastic.
- Rotary inertia is negligible.
- Shear deformation is negligible.

The following differential equation represents the motion of the beam with small deflections, see Appendix A.1, Eq. (A.20) and [15], [16]

$$EI \frac{\partial^4 W}{\partial x^4} - T \frac{\partial^2 W}{\partial x^2} + m_b \frac{\partial^2 W}{\partial t^2} = 0 \tag{27}$$

where $W = W(x,t)$ is the displacement of the beam in the $\boldsymbol{e}_y$-direction, see Figure 9; E is modulus of elasticity in $[Pa]$; I is the second moment of area around the $\boldsymbol{e}_z$-axis of the beam cross section $[m^4]$, the frame is based on a right handed orthonormal basis defined by (O, e_x, e_y, e_z); m_b is the mass per unit length of the beam $[kg/m]$; x is the coordinate in the $\boldsymbol{e}_x$-direction $[m]$; t is the time $[s]$ and T is the axial preload in the $[N]$, which is considered to be positive.

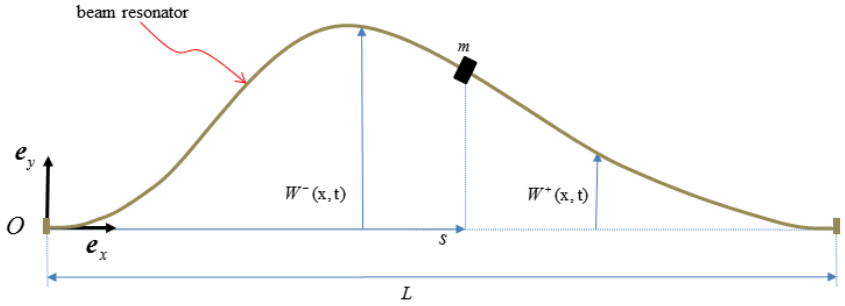

Figure 9. A clamped-clamped beam resonator carrying a sliding proof-mass.

The analytical study of the beam is based on a beam with constant cross-section area and density, leading to the conclusion that m_b is constant. Gravity is neglected.

To solve the differential equation given in Eq. (27) the following harmonic solution is assumed

$$W = W(x,t) = \hat{W}(x)\sin\omega t \tag{28}$$

Then, by combining the harmonic solution in Eq. (28) with the differential equation (27) and introducing the beam non-dimensional coordinate $\zeta(x) = \frac{x}{L}$, the general solutions $\hat{W} = \hat{W}(x)$ is given by

$$\begin{cases} \hat{W}^-(x) = a\sin(N\zeta) + b\cos(N\zeta) + c\sinh(M\zeta) + d\cosh(M\zeta), & 0 \le x \le s \\ \hat{W}^+(x) = e\sin(N\zeta) + f\cos(N\zeta) + g\sinh(M\zeta) + h\cosh(M\zeta), & s \le x \le L \end{cases} \tag{29}$$

where the position of the sliding mass in the $\boldsymbol{e}_x$-direction is denoted by s, the modal coefficients are denoted by a, b, c, d, e, f, g, h and M, N are defined by

$$\begin{aligned} M &= L\left\{-(T/2EI) + \left[(T/2EI)^2 + (\rho A/EI)\omega^2\right]^{1/2}\right\}^{1/2} = (-U + \sqrt{U^2+\Omega^2})^{1/2} \\ N &= L\left\{(T/2EI) + \left[(T/2EI)^2 + (\rho A/EI)\omega^2\right]^{1/2}\right\}^{1/2} = (U + \sqrt{U^2+\Omega^2})^{1/2} \end{aligned} \tag{30}$$

with the dimensionless parameters U and Ω describing the relative axial force and the relative natural frequency respectively ([15],[16]), are defined by

$$U = \frac{TL^2}{2EI}, \quad \Omega = \frac{\omega L^2}{\alpha} \tag{31}$$

where

$$\alpha = \sqrt{\frac{EI}{\rho A}} \tag{32}$$

To assign boundary conditions for the problem in Eq.(27) - (29), we use the same method as with the string, dividing the beam in two parts with one fixed point at each side and connecting the two sides to each other at the other point, $[-]\ 0 \le x \le s$,and $[+]\ s \le x \le L$, where $x = s$ is the position of the sliding-mass on the beam and also specifying where the two hypothetical sides are connected, see Figure 9.

There are eight boundary conditions obtained for the beam with sliding-mass system. The first four are related to the fixed ends of the beam. Due to the fact that it is a clamped-clamped beam, there is no linear displacement at the beam ends, leading to

$$\hat{W}^{-}(0) = 0, \quad \hat{W}^{+}(L) = 0 \tag{33}$$

and neither is there any angular displacements at the fixed ends

$$\frac{d\hat{W}^{-}}{dx}(0) = 0, \quad \frac{d\hat{W}^{+}}{dx}(L) = 0 \tag{34}$$

The last four boundary conditions are associated with the two parts of the beam were the sliding proof-mass is located at point $x = s$. The first of those are for the vertical displacement at each side of the connecting point and they must be equal

$$\hat{W}^{-}(s) = \hat{W}^{+}(s) \tag{35}$$

the second one is for the angular displacement at the connecting point and also that must be the same for the two sides

$$\frac{d\hat{W}^{-}}{dx}(s) = \frac{d\hat{W}^{+}}{dx}(s) \tag{36}$$

the third boundary condition concerning the connection point is for the bending moment and the bending moment at each side of the point *s* is equal

$$\frac{d^2\hat{W}^-}{dx^2}(s) = \frac{d^2\hat{W}^+}{dx^2}(s) \tag{37}$$

For the fourth and last boundary condition concerning the connection point, the following equilibrium relationship of the shear forces at the point $x = s$ is set up.

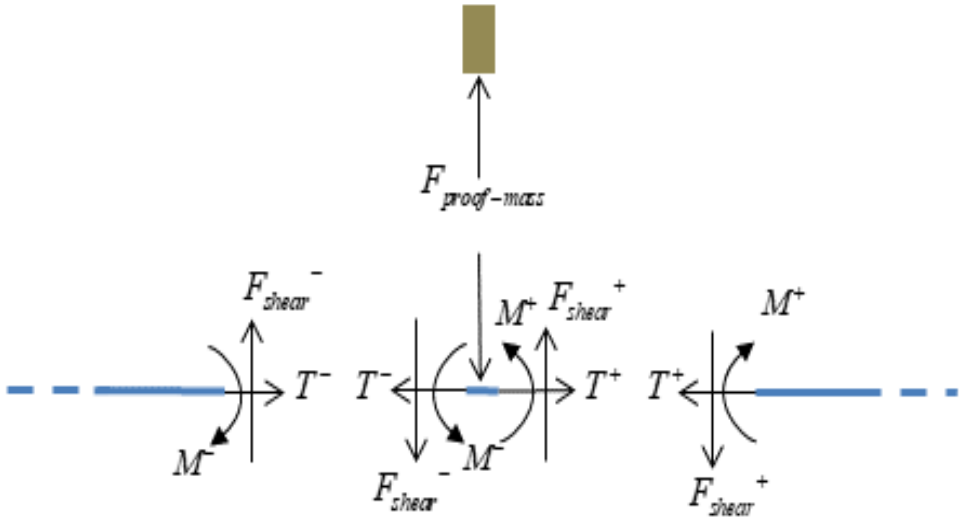

Figure 10. Free body diagram at point $x = s$ on the beam.

$$(\uparrow): \quad F_{shear}^+ - F_{shear}^- - F_{proof-mass} = 0 \tag{38}$$

where $F_{proof-mass}$ satisfies the equation

$$F_{proof-mass} = m\frac{\partial^2 W}{\partial t^2}(s,t) = -m\omega^2\hat{W}(s)\sin\omega t \tag{39}$$

and F_{shear} the shear force at each side of the beam described as

$$\begin{cases} F_{shear}^- = \dfrac{\partial M^-}{\partial x} + T\dfrac{\partial W^-}{\partial x} = -EI\dfrac{d^3\hat{W}^-}{dx^3} + T_0\dfrac{d\hat{W}^-}{dx} \\ F_{shear}^+ = \dfrac{\partial M^+}{\partial x} + T\dfrac{\partial W^+}{\partial x} = -EI\dfrac{d^3\hat{W}^+}{dx^3} + T_0\dfrac{d\hat{W}^+}{dx} \end{cases} \tag{40}$$

Inserting Eq.(39) and Eq.(40) in the equilibrium equation (38) will give us the following expression for the eighth and last boundary condition of our problem

$$-EI\frac{d^3\hat{W}^-}{dx^3}(s)+T_0\frac{d\hat{W}^-}{dx}+EI\frac{d^3\hat{W}^+}{dx^3}(s)-T_0\frac{d\hat{W}^+}{dx}=-m\omega^2\hat{W}(s) \qquad (41)$$

Eq. (29) together with the eight boundary conditions can be set up in a matrix format. But, due to the boundary conditions specified in Eq. (33) and Eq.(34), this leads to $d=-b$ and $c=-a\frac{N}{M}$. It is now possible to represent the boundary conditions with a 6x6-matrix as follows.

$$\underbrace{\begin{pmatrix} J_1-\frac{N}{M}J_3 & J_2-J_4 & -J_1 & -J_2 & -J_3 & -J_4 \\ NJ_2-J_4 & -NJ_1-MJ_3 & -NJ_2 & NJ_1 & -MJ_4 & -MJ_3 \\ -N^2J_1-MNJ_3 & -N^2J_2-M^2J_4 & N^2J_1 & N^2J_2 & -M^2J_3 & -M^2J_4 \\ Z_1J_2+\frac{N}{M}Z_2J_4-\omega\left(J_1-\frac{N}{M}J_3\right) & -Z_1J_1+Z_2J_3-\omega\left(J_2-J_4\right) & -Z_1J_2 & Z_1J_1 & Z_2J_4 & Z_2J_3 \\ 0 & 0 & \sin N & \cos N & \sinh M & \cosh M \\ 0 & 0 & \frac{N}{L}\cos N & -\frac{N}{L}\sin N & \frac{M}{L}\cosh M & \frac{M}{L}\sinh M \end{pmatrix}}_{=A}\begin{pmatrix} a \\ b \\ e \\ f \\ g \\ h \end{pmatrix}=\begin{pmatrix} 0 \\ 0 \\ 0 \\ 0 \\ 0 \\ 0 \end{pmatrix}$$

(42)

in which

$$\begin{cases} J_1=\sin N\zeta_s,\ J_2=\cos N\zeta_s,\ J_3=\sinh M\zeta_s,\ J_4=\cosh M\zeta_s, \\ Z_1=EI\left(\frac{N}{L}\right)^3,\ Z_2=EI\left(\frac{M}{L}\right)^3 \end{cases} \qquad (43)$$

where $\zeta_s=\zeta(s)=s/L$ in Eq. (43).

Finally, the eigenfrequency of the whole system, including the beam and the sliding proof-mass, will be obtained by calculating the determinant of the matrix *A* given in Eq. (42) and solving the characteristic equation.

$$\det A=0 \qquad (44)$$

When studying a beam without any axial load, we put $T=0$ in Eq.(27) and we will get the following differential equation

$$EI\frac{\partial^4 W}{\partial x^4} + m_b \frac{\partial^2 W}{\partial t^2} = 0 \tag{45}$$

Rewriting Eq.(45), with the harmonic solution in Eq.(28), gives us the following equation

$$\frac{d^4 \hat{W}}{dx^4} - \mu^4 \hat{W} = 0 \tag{46}$$

where

$$\mu^4 = \frac{\omega^2 m_b}{EI} \tag{47}$$

this will lead to the following general solution

$$\begin{cases} \hat{W}^-(x) = a\sin(\mu x) + b\cos(\mu x) + c\sinh(\mu x) + d\cosh(\mu x), \ 0 \le x \le s \\ \hat{W}^+(x) = e\sin(\mu x) + f\cos(\mu x) + g\sinh(\mu x) + h\cosh(\mu x), \ s \le x \le L \end{cases} \tag{48}$$

When specifying the boundary value problem we use almost the same boundary conditions as earlier, that is, Eq.(33), (34), (35), (36) and (37), except for the eighth and final one, that now does not include any pre-stress.

We put up a new equilibrium equation

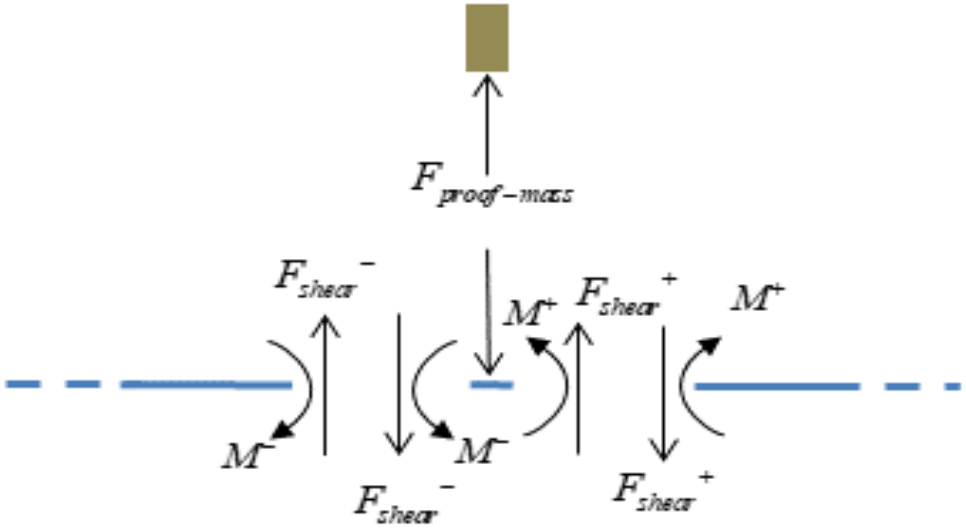

Figure 11. Free body diagram at point $x = s$ on the beam without preload I the normal force.

$$F_{proof-mass} + F_{shear}^{-} - F_{shear}^{+} = 0 \tag{49}$$

where $F_{proof-mass}$ is still the same

$$F_{proof-mass} = m\frac{\partial^2 W}{\partial t^2}(s,t) = -m\omega^2 \hat{W}(s)\sin\omega t \tag{50}$$

but now the shear force F_{shear} is

$$\begin{cases} F_{shear}^{-} = \dfrac{\partial M^{-}}{\partial x} = -EI\dfrac{d^3\hat{W}^{-}}{dx^3}(s) \\ F_{shear}^{+} = \dfrac{\partial M^{+}}{\partial x} = -EI\dfrac{d^3\hat{W}^{+}}{dx^3}(s) \end{cases} \tag{51}$$

which will lead to this new and simpler eighth boundary condition

$$EI\frac{d^3\hat{W}^{+}}{dx^3}(s) - EI\frac{d^3\hat{W}^{-}}{dx^3}(s) = m\omega^2\hat{W}(s) \tag{52}$$

Setting up a new system of linear equations for this new problem we get

$$
\underbrace{\begin{pmatrix}
J_1 - J_3 & J_2 - J_4 \\
J_2 - J_4 & -J_1 - J_3 \\
-J_1 - J_3 & -J_2 - J_4 \\
\left(J_2 + J_4\right) - \dfrac{m}{m_b}\mu\left(J_1 - J_3\right) & -\left(J_1 - J_3\right) + \dfrac{m}{m_b}\mu\left(J_2 - J_4\right) \\
0 & 0 \\
0 & 0
\end{pmatrix}}_{=A}
\begin{pmatrix}
-J_1 & -J_2 & -J_3 & -J_4 \\
-J_2 & J_1 & -J_4 & -J_3 \\
J_1 & J_2 & -J_3 & -J_4 \\
-J_2 & J_1 & J_4 & J_3 \\
\sin \mu L & \cos \mu L & \sinh \mu L & \cosh \mu L \\
\cos \mu L & -\sin \mu L & \cosh \mu L & \sinh \mu L
\end{pmatrix}
\begin{pmatrix} a \\ b \\ e \\ f \\ g \\ h \end{pmatrix}
= \begin{pmatrix} 0 \\ 0 \\ 0 \\ 0 \\ 0 \\ 0 \end{pmatrix}
\tag{53}
$$

in which

$$
\begin{cases}
J_1 = \sin \mu s,\ J_2 = \cos \mu s,\ J_3 = \sinh \mu s,\ J_4 = \cosh \mu s \\
\mu = \sqrt[4]{\dfrac{\omega^2 m_b}{EI}}
\end{cases}
\tag{54}
$$

where the eigenfrequency of this system also be obtained by calculating the determinant of the matrix A given by Eq. (53) and solving the characteristic equation

$$
\det A = 0 \tag{55}
$$

3.2.3 Sliding-mass

The analytical work for the sliding-mass has been done earlier in Miller [13] where the equation of motion for the sliding-mass in the $\boldsymbol{e}_x$-coordinate is described by the following equation

$$
0 = m\ddot{s} + m(\ddot{W}_0 + \ddot{W} + 2\dot{W}'\dot{s} + W''\dot{s}^2 + W'\ddot{s})W' \tag{56}
$$

where m is the sliding proof-mass; $x = s(t)$ is the position of the sliding proof-mass in the $\boldsymbol{e}_x$- direction; $W_0(t)$ is the excitation of the system; $W(s(t),t)$ is the position of the sliding proof-mass in the $\boldsymbol{e}_z$-direction. In Eq.

(56), the dots denotes derivative with respect to time and prime denotes derivative with respect to x. Eq. (52) may be written

$$m(1+W'^2)\ddot{s} = -m(\ddot{W}_0 + \ddot{W} + 2\dot{W}'\dot{s} + W''\dot{s}^2)W' \tag{57}$$

From Eq. (56), it can be observed that when the slope W' is zero, there is no driving force on the sliding-mass. In Appendix A.2 the conditions for the beam and the proof-mass at $x = s(t)$ are derived. The resulting equations are complicated and a solution involving the beam motion and the motion of the proof mass is not considered in this thesis.

3.3 Modal analysis

A numeric study, based on the analytical models developed in the previous chapters, is presented. The study is based on the characteristics of a reference steel beam given in Table 1 [12].

Table 1. Characteristics of the reference steel beam [12].

Parameter	Value	Unit
Beam length	L = 0.060	m
Beam width	b = 0.003	m
Beam thickness	h = 0.0001	m
Beam mass	m_b = 0.14	g
Proof mass	m = 0.8	g
Elastic modulus	E = 200	GPa
Second moment of area	I = 2.5E -16	m^4

3.3.1 String

In the study of the string-mass system the pretension required for the string is derived by setting the first eigenfrequency of the string the same as for the reference steel beam, which will give us a string-mass system comparable to the beam-mass system. We set the length and mass of the string the same as for the reference beam. The pretension required for the system can be conducted from the following equation.

$$\omega_n = n\pi\sqrt{\frac{T_0}{m_{0b}L^2}} \tag{58}$$

Solving Eq (58)

$$T_0 = \left(\frac{\omega_n}{\pi n}\right)^2 m_{0b} L^2 = 0.7044 \text{ Nm} \tag{59}$$

where $m_{0b} = 0.00014/0.06$ [Kg/m] is the mass per unit length of the beam, $L = 0.06$ [m] the length of the beam which should correspond with the length of the string and $\omega_1 = 909.7$ [rad/s] the natural frequency of the reference beam for the first mode. For the following numerical study of the string the pretension, $T_0 = 0.7044$ Nm unless otherwise is mentioned.

Inserting the modal coefficients obtained from equation (25) in equations (15) and boundary conditions in equation (16) will enable the plotting of the mode shapes for different eigenfrequencies at different mass positions and to evaluate the range of resonance frequency for the string-system. In the case for the sliding-mass placed at the mid-point of the string the first eigenfrequency was 235.4 rad/s. When the sliding-mass was placed at one of the ends of the string the first eigenfrequency was 909.7 rad/s which is the same frequency as for a string without any sliding-mass. In Figure 12 the first mode shapes for the two cases are presented, where it can be observed how the peak of the mode shape gets distinctly sharper in the case were the sliding-mass is placed

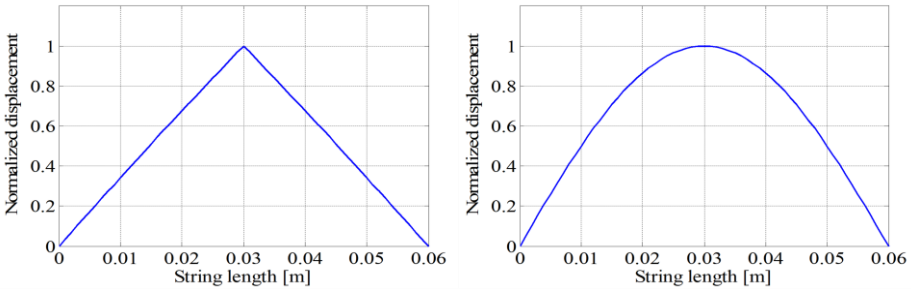

Figure 12. The first mode shape of the string when the sliding mass is placed at the midpoint of the string, $s = 0.03m$ (left), and when the sliding mass is at the endpoint of the string, $s = 0m$ or $s = 0.06m$ (right).

at the mid-point of the string.

The second eigenfrequency for the string system with the sliding-mass placed at the string midpoint occurs at the excitation frequency 2507.7 rad/s and it is the same frequency for the string system when the sliding-mass is placed at

one of the endpoints. As seen in Figure 13 the mode shapes for the two cases will be identical since the position of the sliding mass at the string midpoint is a stationary point for the second mode and will not have any effect on the second eigenfrequency of the model.

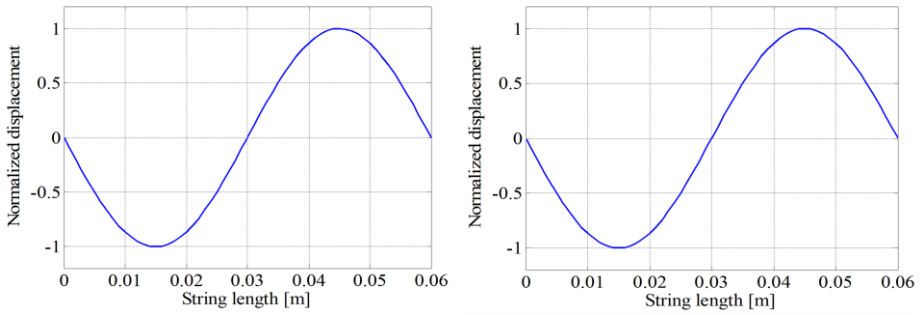

Figure 13. The 2nd mode shape of the string when the sliding mass is placed at the midpoint of the string, $s = 0.03m$ (left), and when the sliding mass is at the endpoint of the string, $s = 0m$ or $s = 0.06m$ (right).

The first mode shapes for the string-system when the sliding-mass is positioned other than the ends or the mid-point of the string can be observed in Figure 14 and Figure 15. It is also possible to observe that the peak points of the first mode shapes are in parallel with the position of the sliding-mass and continues to have the distinctive shape, with a sharp peak point.

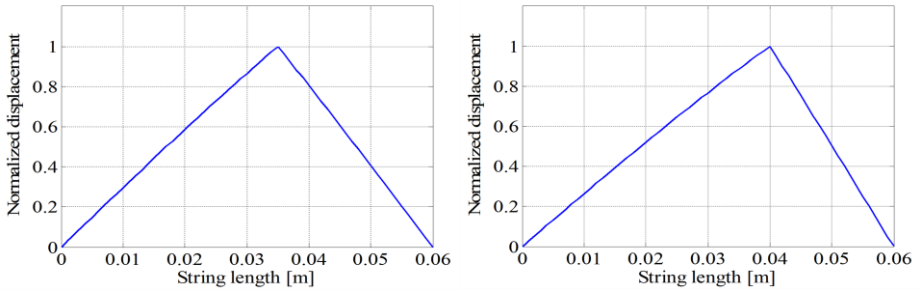

Figure 14. The first mode shape of the string when the sliding mass is placed at $s = 0.035m$ (left), and when the sliding mass is placed at $s = 0.04m$ (right).

The string has a symmetric behavior within the resonance frequency range, in terms of sliding-mass position, it is the same for both sides of the string midpoint. The lowest eigenfrequency is achieved when the sliding-mass is positioned at the midpoint of the string and the largest is obtained when the

sliding-mass is at either ends of the string. The range of the resonance frequency is given in Figure 16.

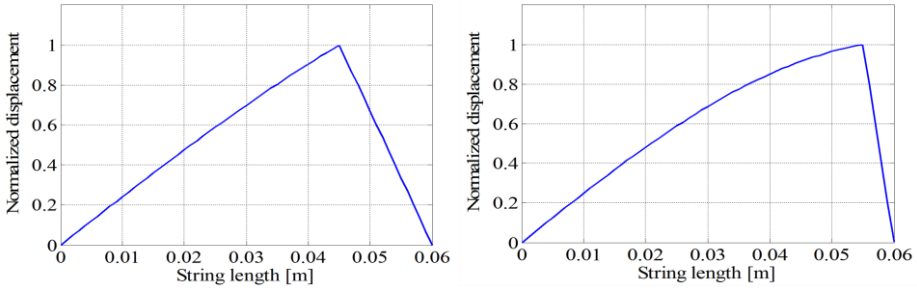

Figure 15. The first mode shape of the string when the sliding mass is placed at $s = 0.045m$ (left), and when the sliding mass is placed at $s = 0.055m$ (right).

The string has a symmetric behavior within the resonance frequency range, in terms of sliding-mass position, it is the same for both sides of the string midpoint. The lowest eigenfrequency is achieved when the sliding-mass is positioned at the midpoint of the string and the largest is obtained when the sliding-mass is at either ends of the string. The range of the resonance frequency is given in Figure 16.

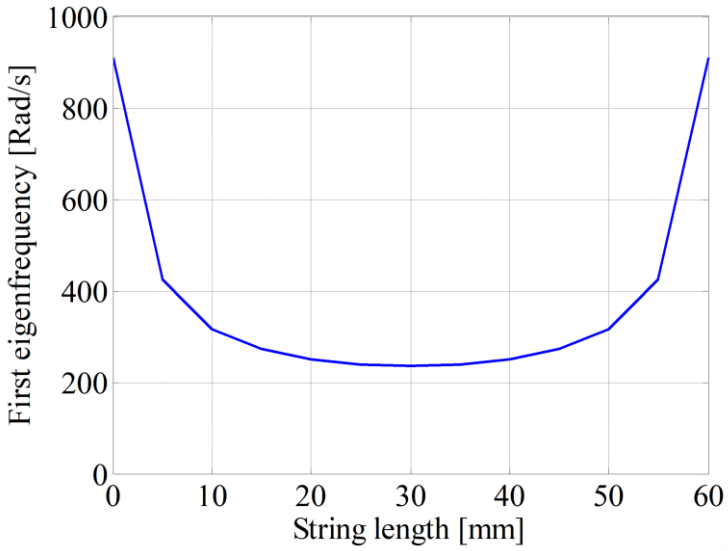

Figure 16. The first eigenfrequency range in terms of the position of the sliding-mass for the string-system.

3.3.2 Beam

Inserting the modal coefficients obtained from equation (42) in equations (29) and with the boundary conditions in equations (33) and (34), enables the plotting of the mode shapes for different eigenfrequencies at different mass positions. In this numeric study, the range of resonance frequency and the effect of preload on resonance frequency are evaluated.

The first mode shape, for the beam with the sliding-mass placed at the midpoint of the beam and for the beam with the sliding-mass placed at one end of the beam is presented in Figure 17.

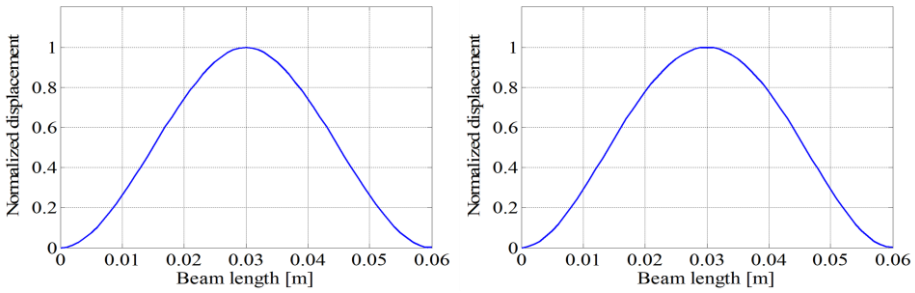

Figure 17. The first mode shape of the beam when placing the sliding-mass at the midpoint of the beam, $s = 0.03m$ (left), and when the sliding mass is placed at one end of the beam (right).

The second mode shapes, for the beam with the sliding-mass placed at the midpoint of the beam and for the beam with the sliding-mass placed at one end of the beam, are presented in Figure 18. As for the string model, the mode shape for the beams with the sliding mass placed at the midpoint and the ends will be identical since the position of the sliding mass at the beam midpoint is a stationary point for the second mode and will not have any effect on the second eigenfrequency of the model.

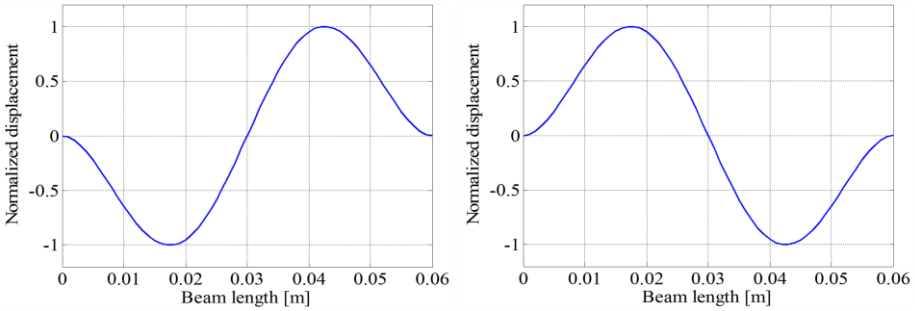

Figure 18. The second mode shape of the beam when placing the sliding-mass at the midpoint of the beam, $s = 0.03m$ (left), and when the sliding mass is placed at one end of the beam (right).

When positioning the sliding-mass other than the ends or the midpoint of the beam, a skewness can be observed. In Figure 19 this skewness can be observed for the first mode shape of the beam with the sliding mass placed at two different positions.

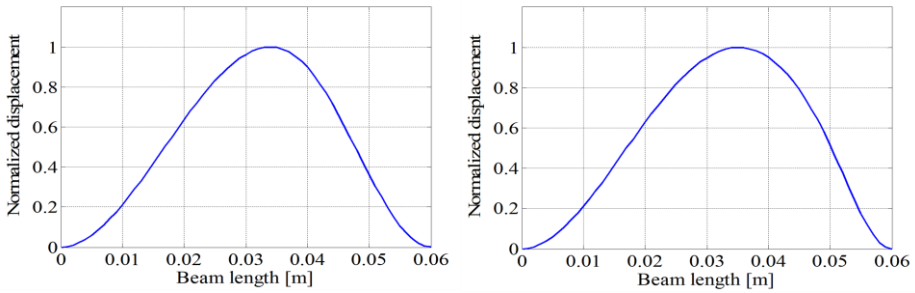

Figure 19. The first mode shape of the beam when placing the sliding-mass at $s = 0.04m$ (left), and when the sliding mass is placed at $s = 0.05m$ (right).

When applying a pretension of $3N$ to the beam system the first eigenfrequency of the system gets higher. In addition to the rise in the first eigenfrequency, as can be seen in Figure 20 the peaks of the mode shapes move towards the end of the beam and become sharper at the peak points.

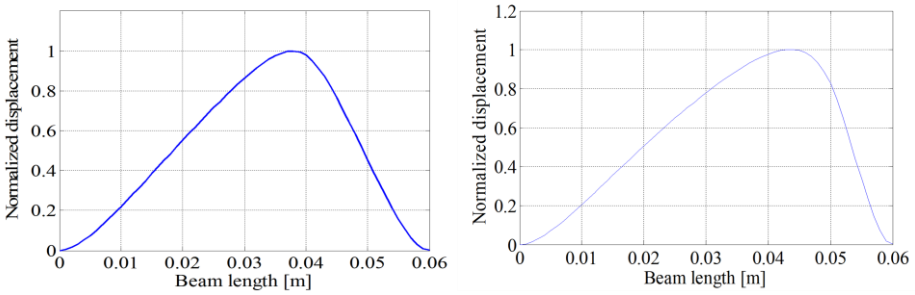

Figure 20. The first mode shape of the beam when there is pretension $T = 3N$ with the sliding-mass at $s = 0.04m$ (left), and when the sliding mass is placed at $s = 0.05m$ (right).

If precompression is applied to the beam-system a decrease in the first eigenfrequency will occure. The peaks of the mode shape move toward the center of the beam and become more flattened compared to the case with the beam with pretension. The beam mode shapes with precompression

$T = -0.2N$ at two different locations of the sliding-mass can be seen in Figure 21.

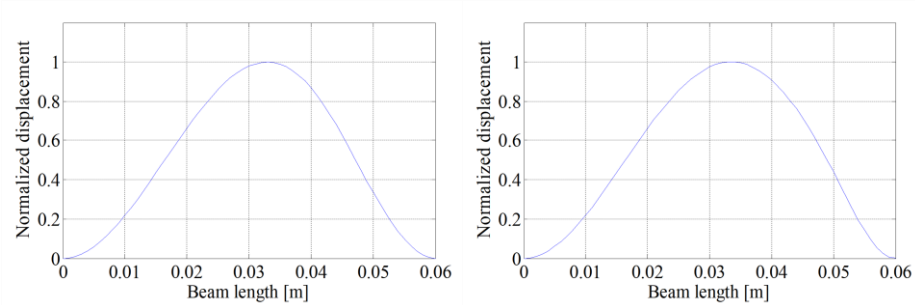

Figure 21. The first mode shape of the beam when there is precompression $T = -0.2N$ with the sliding-mass at $s = 0.04m$ (left), and when the sliding mass is placed at $s = 0.05m$ (right).

From the first mode shapes for the beam with pretension and precompression it is possible to draw the conclusion that preloading is an important desig factor. Preloading can influence the mode shapes as well as the first eigenfrequency. In Figure 22, the first eigenfrequency in terms of the preload is presented where the sliding-mass is positioned at $s = 0.040m$ and $s = 0.050m$. It is also shown that buckling occures where the first eigenfrequency approaches zero at $T \cong -0.548N$ corresponding with the results that can be obtained from the theory of buckling.

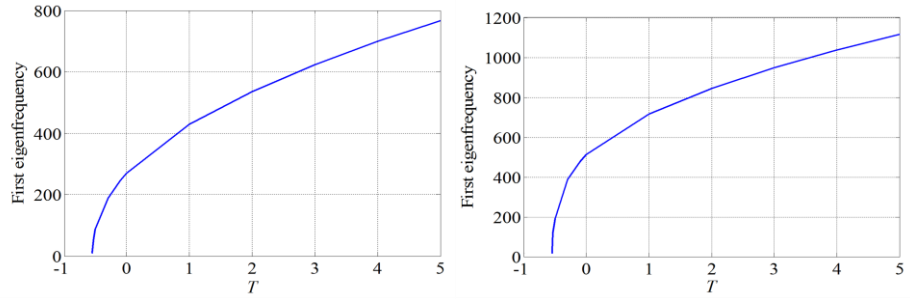

Figure 22. Influence of preload on the first eigenfrequency: when the sliding-mass at $s = 0.04m$ (left), and when the sliding mass is placed at $s = 0.05m$ (right).

The first eigenfrequency range for the beam-system is given in Figure 23. Like for the string-model the symetric behavior is clearly shown with the minimum value for the first eigenfrequency is achived when the sliding-mass is at the midpoint of the beam. The maximum is achived when the sliding-mass is at

either ends of the beam. The ranges of the first eigenfrequency when there is a pretension ($T = 3N$) and a precompression ($T = -0.2N$) are also shown in Figure 23.

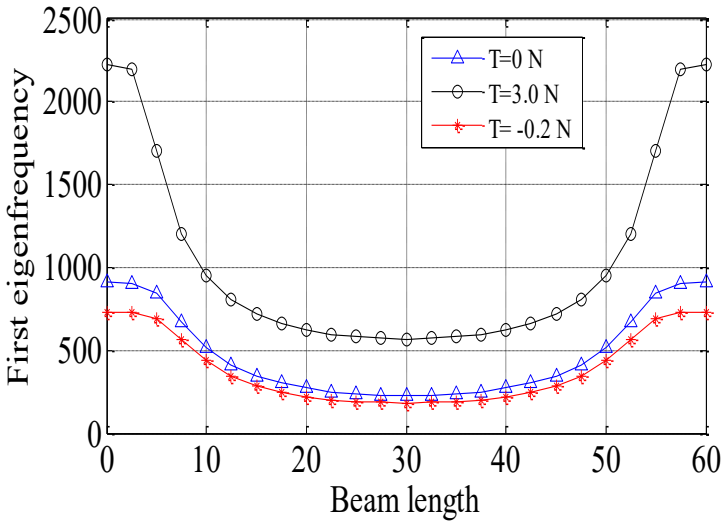

Figure 23. First eigenfrequency range in terms of sliding-mass position for three different preloads.

3.4 Simulation models

3.4.1 Adams

Adams is one of the world´s most widely used multibody dynamics software that helps to understand the dynamics of systems with moving parts [17]. A great work was made trying to simulate the behavior of the clamped-clamped beam with sliding-mass system in Adams.

The Beam was modeled as a *rigid body link* fixed at both ends with a *fixed joint*. *Rigid body link* is a part that has mass and inertia and cannot deform. To make the modeled beam able to bend when forces are applied to it, the beam is transformed into a *"Flexible Body"* during the meshing procedure in Adams. The fixture with the fixed beam was fixed with a *translational joint* that applied the sinusoidal oscillating motion and prevented any other movement than vertical. The sliding-mass was modeled as a rigid body with an extrusion enabling the movement along the beam possible. With a translational joint on the sliding mass preventing any other movement than along the beam length. The *Contact surface* feature defined the contact properties between the surfaces on the extrusion of the sliding-mass and the beam surface. In the contact surface feature, it was possible to set the coefficient of friction and the

relative damping between the two surfaces. A design of experiments procedure where conducted to test different values for the coefficient of friction and the relative damping.

There were a lot of complexity and capacity setbacks that uncured during the simulations of the self-tuning beam resonator. The main obstacle was the hardware's ability to process the simulation of the system. With the need of at least three elements across the thickness of the beam and a beam-model with 0.1 mm in thickness gave an element size smaller than 0.034 mm. That made the total element amount for the beam a lot higher than what the available hardware could process. That prevented the possibility to get any finished simulations of a beam with tree elements along its thickness since the hardware limitation occurred already at the meshing procedure. The simulations made with a beam model with fewer elements than three across the thickness gave incorrect results and had to be disregarded. Attempts to rescale the model and to modify the geometry of the beam where made. But it was not possible to recreate the results from the experiments presented by Miller et al.[12].

MSC Software's were contacted to help us in our simulation problem. They recommended us to use the new feature *FE-part* in the updated version of Adams. Since with the *FE-part* feature, we could design a beam with the ability to bend without transforming it to flexible part thru the meshing procedure. In collaboration with the engineers at MSC Software's a new model was designed with the feature *FE-part* in Adams, shown in Figure 24.

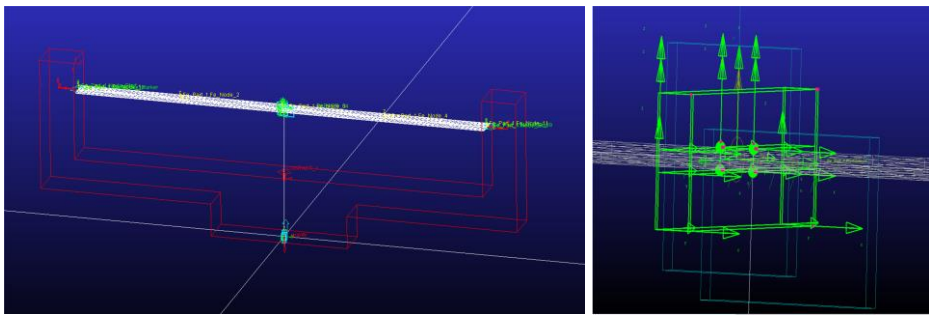

Figure 24. The Beam as an FE-part connected to the fixture (left), and the sliding-mass (right).

A construction where made with an FE-part as a beam. A fixed joint is connecting each end of the beam to a fixture that has a translational joint connected to it, producing a sinusoidal oscillating motion for the entire model. For the sliding-mass, two plates with four half spheres where used with a contact surface between the spheres and the FE part, to minimize the contact surface. A translational joint was added to the sliding mass to prevent any

other sliding motion then across the beam length. Numerous experiments were made with different inputs to the friction and contact stiffness and damping parameters. Unfortunately, no valid results could be extracted due to the unverified behavior of the system. There was insufficient knowledge of the nonlinear behavior of the FE-part. MSC Software was contacted once again to assist in understanding the FE-part, but no further success could be achieved from their part. A reproduction of the experimental behavior in Adams was not possible, mainly due to the systems complex behavior under nonlinearity.

3.4.2 Nonlinear ABAQUS® simulation

A new attempt was made simulating the behavior of the self-tuning beam resonators with sliding-mass, so a clamped-clamped beam with a sliding-mass is modeled in ABAQUS® together with Behrouz Afzali Far. For the shortest possible run-time of the program, the model is constructed two-dimensionally with an assigned beam profile. The simulation is done using dynamic explicit with automatic time increments and *double analysis + packager* precision. The element type is set to be a *2-node linear beam in plane* (B21) which is a Timoshenko beam. Boundary conditions are specified including the harmonic excitation in y-direction applied on either end of the beam

For the contact between the beam and the sliding-mass, two contact properties are defined. First, tangential behavior settings are based on the isotropic penalty formulation with the friction coefficient $\mu = 0.01$ shown in Figure 25 and $\mu = 0.02$ shown in Figure 26. Second, normal behavior setting is pressure-overclosure and set to *hard* contact. The simulation is done based on a reference experimental system given in Table 1. Two cases are studied with different coefficients of friction. The starting position of the proof mass is $s = 0.050m$ and the excitation frequency is 502.65 rad/s. The simulation is done nonlinearly with large deformation effects (NLgeom = on).

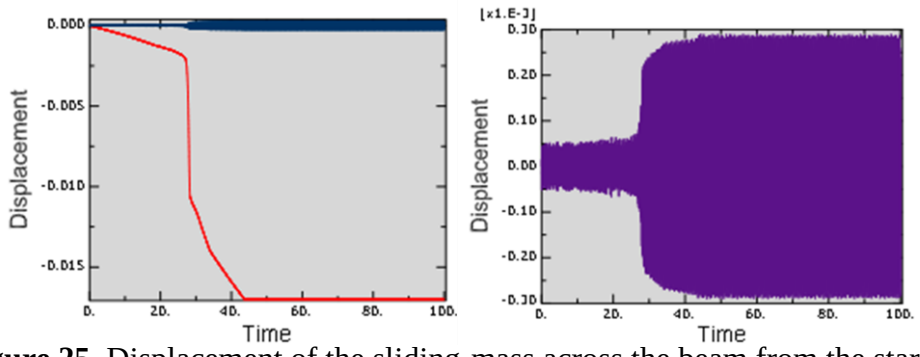

Figure 25. Displacement of the sliding-mass across the beam from the starting position (left) and the displacment of the center of the beam (right). When, $\mu = 0.01$ and $T = 0$.

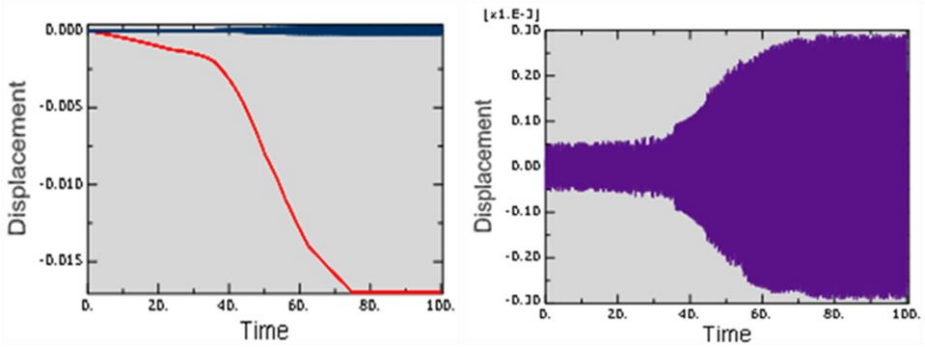

Figure 26. Displacement of the sliding-mass across the beam from the starting position (left) and the displacment of the center of the beam (right). When, $\mu = 0.02$ and $T = 0$.

4 Conclusions and future work

Earlier work on the self-tuning beam and string resonators with sliding-mass showed via experiments the distinct tuning behavior of those systems, in this thesis, a computer-aided simulation reproduced the results from those experiments and could confirm the behavior. Also, analytical models of the self-tuning beam and string resonators with sliding-mass have been developed. A numerical study based on those models showed the natural frequency range the systems could cover and the possibility of using preload to modify and broaden the bandwidth and the mode shapes. Also, that pretension is useful to increase the speed of the system to reach resonance. The results have shown that the self-tuning beam and string resonators, with sliding-mass, has great potential due to its capability to increase the natural frequency range of vibration energy harvesting generators. This makes it possible to harvest energy from wearable devices, industrial machines or other applications with an operational frequency that is not homogenous.

For future work, collect real experimental results on downscaled variants of the system, and the use of different material for the beam.

References

[1] Y.K. Tan, W.S. Koh, Wearable Energy Harvesting System for Powering Wireless Devices, (2011).

[2] L. Tang, Y. Yang, C.K. Soh, Advances in Energy Harvesting Methods, Springer New York, New York, NY, 2013. doi:10.1007/978-1-4614-5705-3.

[3] L. Xie, C.G. Menet, H. Ching, R. Du, The Automatic Winding Device of a Mechanical Watch Movement and Its Application in Energy Harvesting, J. Mech. Des. 131 (2009) 71005. doi:10.1115/1.3151803.

[4] L.W. Tom J. Kazmierski, Energy Harvesting Systems : Principles, Modelling and Applications, 2011. doi:10.1007/978-1-4419-7566-9.

[5] V.R. Challa, M.G. Prasad, Y. Shi, F.T. Fisher, A vibration energy harvesting device with bidirectional resonance frequency tunability, Smart Mater. Struct. 17 (2008) 15035. doi:10.1088/0964-1726/17/01/015035.

[6] No Title, (n.d.) http://www.memsnet.org/mems/what_is.html.

[7] D. Zhu, Vibration Energy Harvesting : Machinery Vibration , Human Movement and Flow Induced Vibration, (2008).

[8] C.R. Saha, Modelling Theory and Applications of the Electromagnetic Vibrational Generator, Sustain. Energy Harvest. Technol. - Past, Present Futur. (2011) 55–108.

[9] C.B. Williams, R.B. Yates, Analysis Of A Micro-electric Generator For Microsystems, Proc. Int. Solid-State Sensors Actuators Conf. - TRANSDUCERS '95. 1 (1995) 8–11. doi:10.1109/SENSOR, 1995, 717207.

[10] S.P. Beeby, R.N. Torah, M.J. Tudor, P. Glynne-Jones, T. O'Donnell, C.R. Saha, et al., A micro electromagnetic generator for vibration energy harvesting, J. Micromechanics Microengineering. 17 (2007) 1257–1265. doi:10.1088/0960-1317/17/7/007.

[11] A. Boudaoud, Y. Couder, M. Ben Amar, A self-adaptative oscillator, 165 (1999) 159–165.

[12] L.M. Miller, P. Pillatsch, E. Halvorsen, P.K. Wright, E.M. Yeatman, A.S. Holmes, Experimental passive self-tuning behavior of a beam resonator with sliding proof mass, J. Sound Vib. 332 (2013) 7142–7152. doi:10.1016/j.jsv.2013.08.023.

[13] L.M. Miller, Micro-scale piezoelectric vibration energy harvesting: from fixed-frequency to adaptable-frequency devices, 2012.

[14] P. Lidström, LECTURE NOTES ON MECHANICAL VIBRATIONS, Division of Mechanics Lund University Faculty of Engineering, LTH, 2013.

[15] A. Bokaian, Natural frequencies of beams under tensile axial loads, J.

Sound Vib. 142 (1990) 481–498. doi:10.1016/0022-460X(90)90663-K.

[16] A. Bokaian, Natural frequencies of beams under compressive axial loads, J. Sound Vib. 126 (1988) 49–65. doi:10.1016/0022-460X(88)90397-5.

[17] http://www.mscsoftware.com/product/adams.

5 Appendix

This Appendix is a joint work by the author and the supervisor.

5.1 A.1 The beam in plane motion

The beam centre-line is given by $\boldsymbol{r} = \boldsymbol{r}(x,t),\ \ 0 \le x \le L_0,\ \ 0 \le t \le T$, See Figure A.1. It is assumed that

$$\frac{\partial \boldsymbol{r}(x,t)}{\partial x} \neq \boldsymbol{0},\ \ 0 \le x \le L_0,\ \ 0 \le t \le T$$

The velocity and acceleration of the beam centre-line are defined by

$$\boldsymbol{v} = \boldsymbol{v}(x,t) := \frac{\partial \boldsymbol{r}(x,t)}{\partial t},\ \ 0 \le x \le L_0,\ \ 0 \le t \le T$$

and

$$\boldsymbol{a} = \boldsymbol{a}(x,t) := \frac{\partial \boldsymbol{v}(x,t)}{\partial t},\ \ 0 \le x \le L_0,\ \ 0 \le t \le T$$

respectively.

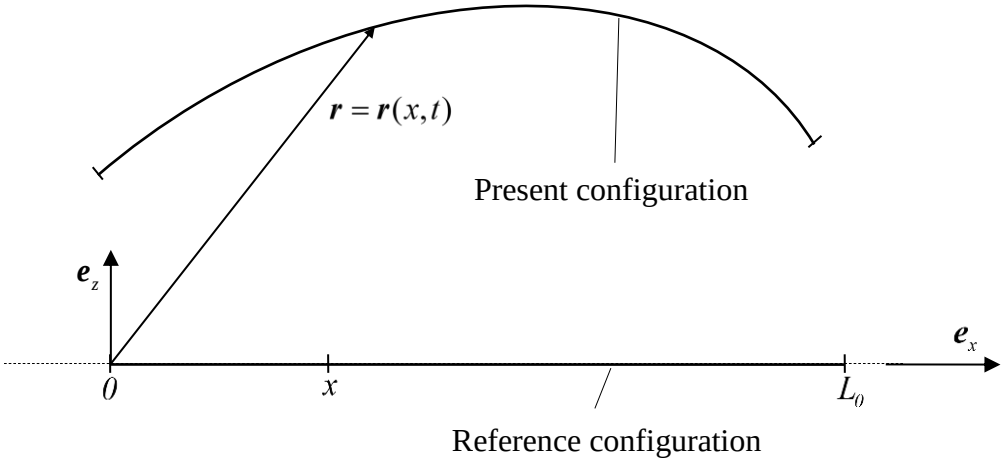

Figure A.1 The beam centre line in its un-deformed and deformed configurations.

We simplify our notation by introducing the following definitions

$$\Phi'(x,t) := \frac{\partial \Phi(x,t)}{\partial x},\ \Phi''(x,t) := \frac{\partial^2 \Phi(x,t)}{\partial x^2},\ \dot{\Phi}(x,t) := \frac{\partial \Phi(x,t)}{\partial t},$$

$$\ddot{\Phi}(x,t) \coloneqq \frac{\partial^2 \Phi(x,t)}{\partial t^2},\ \dot{\Phi}'(x,t) \coloneqq \frac{\partial^2 \Phi(x,t)}{\partial x \partial t} = \frac{\partial^2 \Phi(x,t)}{\partial t \partial x}$$

where $\Phi = \Phi(x,t),\ 0 \le x \le L_0,\ 0 \le t \le T$ is a continuously differentiable scalar or vector valued function. Using this notation we may, for instance, write $\boldsymbol{a}(x,t) = \dot{\boldsymbol{v}}(x,t) = \ddot{\boldsymbol{r}}(x,t)$. The *arc length* of the beam centre-line is defined by

$$s = s(x,t) = \int_0^x \left|\boldsymbol{r}'(q,t)\right| dq$$

Thus $s(0,t) = 0$. We define $L(t) \coloneqq s(L_0,t)$ the length of the beam at time t. The *length ratio*

$$l = l(x,t) \coloneqq s'(x,t) = \left|\boldsymbol{r}'(x,t)\right| > 0$$

For fixed $t \in [0,T]$ we may the invert the function $s = s(x,t)$ and obtain

$$x = x(s,t),\ \ 0 \le s \le L(t),\ \ 0 \le t \le T$$

Thus we may, instead of x,t use s,t and define $\hat{\boldsymbol{r}}(s,t) \coloneqq \boldsymbol{r}(x(s,t),t)$ and then the *unit tangent vector* to the centre-line is given by

$$\boldsymbol{e}_t(s,t) \coloneqq \hat{\boldsymbol{r}}'(s,t) = \boldsymbol{r}'(x(s,t),t)x'(s,t)$$

Since $x'(s,t) = s'(x,t)^{-1} = l(x,t)^{-1}$ we may conclude that $\left|\boldsymbol{e}_t(s,t)\right| = 1$. We have

$$\hat{\boldsymbol{r}}'' = \boldsymbol{e}_t' = \boldsymbol{e}_n \kappa,\ \ \left|\kappa\right| = \left|\hat{\boldsymbol{r}}''\right|$$

where $\boldsymbol{e}_n = \boldsymbol{e}_n(s,t)$ is the main unit normal and $\kappa = \kappa(s,t)$ the curvature of the centre line. The binormal $\boldsymbol{e}_b = \boldsymbol{e}_b(s,t)$ is defined by $\boldsymbol{e}_b = \boldsymbol{e}_b(s,t) \coloneqq \boldsymbol{e}_t(s,t) \times \boldsymbol{e}_n(s,t)$ and the Darboux trihedral $\underline{\boldsymbol{e}} = \left(\boldsymbol{e}_t\ \ \boldsymbol{e}_n\ \ \boldsymbol{e}_b\right)$ constitutes a RON-basis. See Figure A.2. We have the Frenet-Serret formula $\underline{\boldsymbol{e}}' = \boldsymbol{\delta} \times \underline{\boldsymbol{e}}$ where $\boldsymbol{\delta} = \boldsymbol{e}_t \tau + \boldsymbol{e}_b \kappa$ and $\tau = \tau(s,t)$ is the torsion of the centre-line. The Frenet-Serret formula may be written

$$\begin{cases} \boldsymbol{e}_t' = \boldsymbol{e}_n \kappa \\ \boldsymbol{e}_n' = \boldsymbol{e}_t(-\kappa) + \boldsymbol{e}_b \tau \\ \boldsymbol{e}_b' = \boldsymbol{e}_n(-\tau) \end{cases}$$

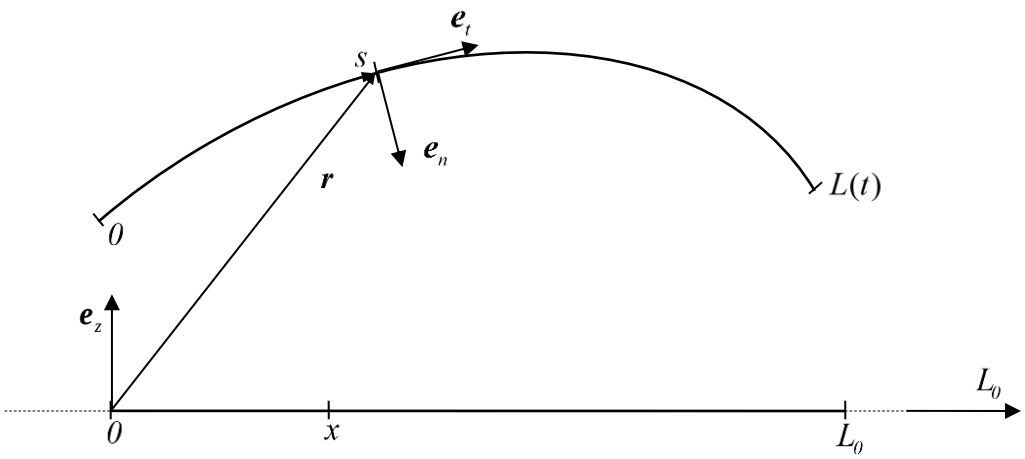

Figure A.2 The beam centre line in its deformed configurations and the Darboux trihedral

The *global balance of momentum* for the part of the beam defined by $0 \le x_1 \le x \le x_2$, see Figure A.3 below.

$$\int_{x_1}^{x_2} \boldsymbol{k}(x,t)dx + \boldsymbol{T}(x_2,t) - \boldsymbol{T}(x_1,t) = \int_{x_1}^{x_2} \boldsymbol{a}(x,t)m(x)dx \qquad \text{(A.1)}$$

where $\boldsymbol{k} = \boldsymbol{k}(x,t)$ is the external force density (per unit length of the beam centre line in its reference configuration),
$\boldsymbol{T} = \boldsymbol{T}(x,t)$ is the sectional force (traction vector),
$\boldsymbol{a} = \boldsymbol{a}(x,t)$ is the acceleration of the beam centre line,
$m = m(x)$ is the mass density of the beam (per unit length of the beam centre line in its reference configuration),

The *global balance of moment of momentum* for the part of the beam defined by $0 \le x_1 \le x \le x_2$, see Figure A.3 below.

$$\int_{x_1}^{x_2} (\boldsymbol{r}(x,t) \times \boldsymbol{k}(x,t) + \boldsymbol{h}(x,t))dx + \boldsymbol{r}(x_2,t) \times \boldsymbol{T}(x_2,t) + \boldsymbol{M}(x_2,t) - \boldsymbol{r}(x_1,t) \times \boldsymbol{T}(x_1,t) -$$

$$\boldsymbol{M}(x_1,t) = \int_{x_1}^{x_2} (\boldsymbol{r}(x,t) \times \boldsymbol{a}(x,t)m(x) + \frac{\partial}{\partial t}(\boldsymbol{I}(x,t)\boldsymbol{\omega}(x,t)))dx \qquad \text{(A.2)}$$

where $\boldsymbol{h} = \boldsymbol{h}(x,t)$ is the external moment density (per unit length of the beam centre line in its reference configuration),
$\boldsymbol{M} = \boldsymbol{M}(x,t)$ is the sectional moment,

$\boldsymbol{I} = \boldsymbol{I}(x,t)$ is the moment of inertia tensor of the beam (per unit length of the beam centre line in its reference configuration) and
$\boldsymbol{\omega} = \boldsymbol{\omega}(x,t)$ is the angular velocity of the beam section, $x \in [0, L_0]$, $t \in [0,T]$.

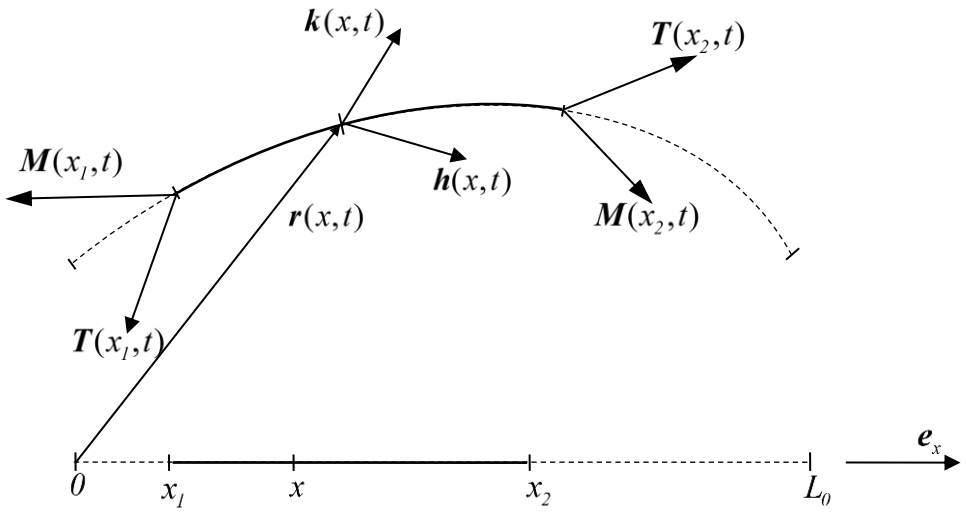

Figure A.3 Part of the beam centre line and the definition of sectional and external forces and moments.

It is assumed that the beam cross-sections perform a rigid motion. The *moment of inertia* of the beam cross-section is given by

$$\boldsymbol{I}(x,t)\boldsymbol{\omega} := \int_{P \in \mathcal{D}(x,t)} \boldsymbol{p}_P(x,t) \times (\boldsymbol{\omega} \times \boldsymbol{p}_P(x,t)) \rho(\boldsymbol{p}_P) da_P$$

where $\rho = \rho(\boldsymbol{p}_P)$ is the cross-section area mass density of the beam and $\boldsymbol{p}_P(s,t) := \boldsymbol{r}_{OP} - \boldsymbol{r}(x,t)$, $P \in \mathcal{D}(x,t)$. See Figure A.4 below. We define

$$m = m(x) := \int_{P \in \mathcal{D}(x,t)} \rho(\boldsymbol{p}_P) da_P$$

The *cross-section area* is given by

$$\mathcal{A}(x) = \int_{P \in \mathcal{D}(x,t)} da_P$$

Since we assume that the beam cross section is moving rigidly we may assume that $\mathcal{A}$ does not depend on t.

The *local equations* of motion, corresponding to (A.1) and (A.2), read

$$\begin{cases} \boldsymbol{k} + \boldsymbol{T}' = \boldsymbol{a}m \\ \boldsymbol{h} + \boldsymbol{r}' \times \boldsymbol{T} + \boldsymbol{M}' = (\dot{\boldsymbol{I}\boldsymbol{\omega}}) \end{cases} \tag{A.3}$$

Now taking

$$\boldsymbol{k} = \boldsymbol{k}(x,t) = \boldsymbol{0}\,,\ \boldsymbol{h} = \boldsymbol{h}(x,t) = \boldsymbol{0},\ x \in [0, L_0],\ t \in [0,T]$$

we have the local equations

$$\begin{cases} \boldsymbol{T}' = \boldsymbol{a}m \\ \boldsymbol{r}' \times \boldsymbol{T} + \boldsymbol{M}' = (\dot{\boldsymbol{I}\boldsymbol{\omega}}) \end{cases} \tag{A.4}$$

where

$$\boldsymbol{T} = \boldsymbol{e}_x T_x + \boldsymbol{e}_y T_y + \boldsymbol{e}_z T_z\,,\ \boldsymbol{M} = \boldsymbol{e}_x M_x + \boldsymbol{e}_y M_y + \boldsymbol{e}_z M_z$$

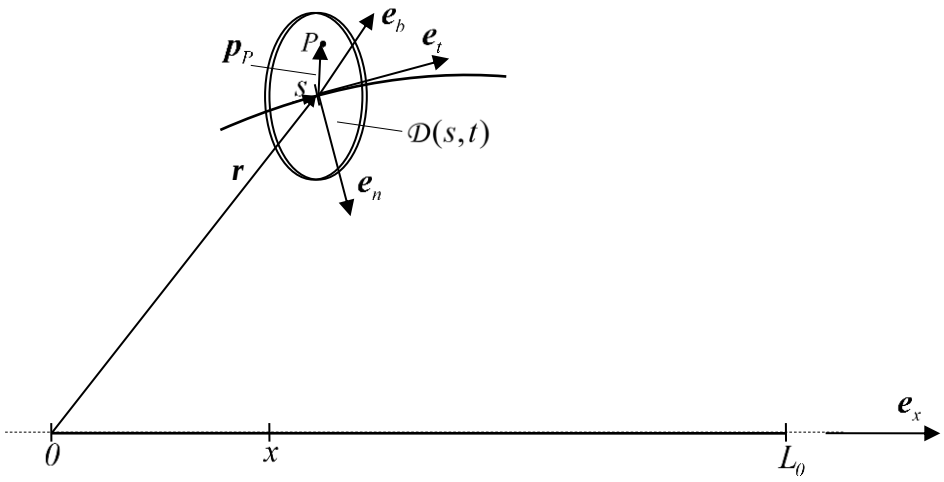

Figure A.4 The beam centre line cross-section.

Consider *plane motion* (in the $\boldsymbol{e}_x$-$\boldsymbol{e}_z$-plane) of the beam centre-line, that is $\boldsymbol{e}_y \cdot \boldsymbol{r}(x,t) = 0,\ x \in [0, L_0],\ t \in [0,T]$. Furthermore we assume that $\boldsymbol{\omega}(x,t) = \boldsymbol{e}_y \omega(x,t)$ where $\boldsymbol{e}_y$ is a principal direction for $\boldsymbol{I}$ then $\boldsymbol{I}\boldsymbol{\omega} = \boldsymbol{I}\boldsymbol{e}_y\omega = \boldsymbol{e}_y I_y \omega$, where $I_y = I_y(x)$. This gives $\frac{d}{dt}(\boldsymbol{I}\boldsymbol{\omega}) = \boldsymbol{e}_y I_y \dot{\omega}$. If we introduce the *displacement* $\boldsymbol{u}(x,t) = \boldsymbol{e}_x u(x,t) + \boldsymbol{e}_z w(x,t)$ then we may write, see Figure A.5,

$$\boldsymbol{r}(x,t) = \boldsymbol{e}_x x + \boldsymbol{u}(x,t) \tag{A.5}$$

and then

$$\boldsymbol{r}' = \boldsymbol{e}_x + \boldsymbol{u}' = \boldsymbol{e}_x(1+u') + \boldsymbol{e}_z w' \,,\ \boldsymbol{r}'' = \boldsymbol{e}_x u'' + \boldsymbol{e}_z w''$$

$$\boldsymbol{r}' \times \boldsymbol{T} = (\boldsymbol{e}_x(1+u') + \boldsymbol{e}_z w') \times (\boldsymbol{e}_x T_x + \boldsymbol{e}_z T_z) = \boldsymbol{e}_y (T_x w' - T_z(1+u'))$$

$$\boldsymbol{a} = \boldsymbol{e}_x \ddot{u} + \boldsymbol{e}_z \ddot{w}$$

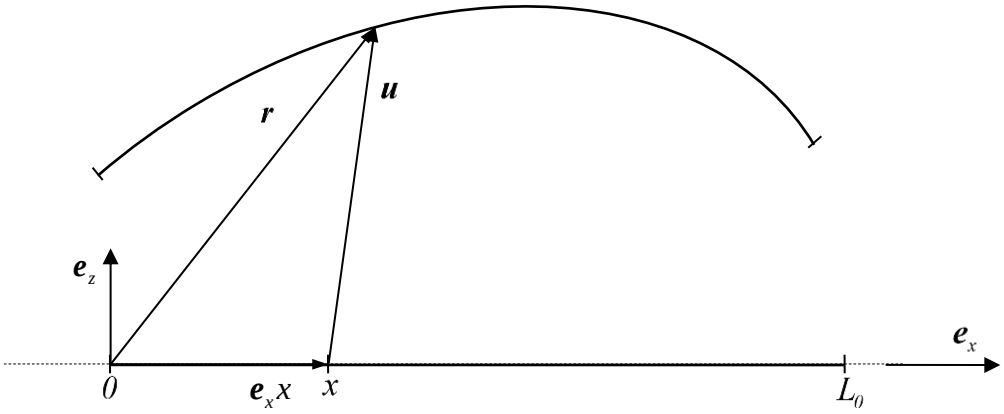

Figure A.5 The beam centre-line displacement.

The equations of motion may now be written

$$\begin{cases} T_x' = \ddot{u}m \\ T_y' = 0 \\ T_z' = \ddot{w}m \\ M_x' = 0 \\ T_x w' - T_z(1+u') + M_y' = I_y \dot{\omega} \\ M_z' = 0 \end{cases} \tag{A.6}$$

We may take, as a solution,

$$T_y = T_y(x,t) = 0 \,,\ M_x = M_x(x,t) = 0 \,,\ M_z = M_z(x,t) = 0,\ x \in [0, L_0],\ t \in [0, T]$$

The remaining equations are

$$\begin{cases} T_x' = \ddot{u}m \\ T_z' = \ddot{w}m \\ T_x w' - T_z(1+u') + M_y' = I_y\dot{\omega} \end{cases} \tag{A.7}$$

From the last equation it follows, after differentiating with respect to x,

$$T_x' w' + T_x w'' - T_z'(1+u') - T_z u'' + M_y'' = (I_y')\dot{\omega} + I_y\dot{\omega}' \tag{A.8}$$

We have the relations

$$\boldsymbol{e}_t = \frac{\boldsymbol{e}_x(1+u') + \boldsymbol{e}_z w'}{\sqrt{(1+u')^2 + (w')^2}},\ \boldsymbol{e}_n = \boldsymbol{e}_y \times \boldsymbol{e}_t = \frac{\boldsymbol{e}_x w' + \boldsymbol{e}_z(-(1+u'))}{\sqrt{(1+u')^2 + (w')^2}}$$

and then

$$\boldsymbol{T} = \boldsymbol{e}_t T_t + \boldsymbol{e}_n T_n = \frac{\boldsymbol{e}_x(1+u') + \boldsymbol{e}_z w'}{\sqrt{(1+u')^2 + (w')^2}} T_t + \frac{\boldsymbol{e}_x w' + \boldsymbol{e}_z(-(1+u'))}{\sqrt{(1+u')^2 + (w')^2}} T_n =$$

$$\boldsymbol{e}_x \frac{(1+u')T_t + w'T_n}{\sqrt{(1+u')^2 + (w')^2}} + \boldsymbol{e}_z \frac{w'T_t + (-(1+u'))T_n}{\sqrt{(1+u')^2 + (w')^2}} = \boldsymbol{e}_x T_x + \boldsymbol{e}_z T_z$$

Thus

$$\begin{cases} T_x = \dfrac{(1+u')T_t + w'T_n}{\sqrt{(1+u')^2 + (w')^2}} \\ T_z = \dfrac{w'T_t - (1+u')T_n}{\sqrt{(1+u')^2 + (w')^2}} \\ M_y = M_b \end{cases} \tag{A.9}$$

We have the *constitutive equations*,

$$T_n(x,t) = \beta G \mathcal{A}(x)(\psi(x,t) - \theta(x,t)),\ T_t(x,t) = E\mathcal{A}(x)\varepsilon(x,t),$$
$$M_b(x,t) = -EJ_y(x)\psi'(x,t) \tag{A.10}$$

where $\dot{\omega} = -\ddot{\psi}$, and $\psi = \psi(x,t)$ is the *rotation angle* of the beam cross-section, see Figure A.6. Furthermore β is the shape factor of the cross-section, G is the shear modulus and E the Young's modulus.

$$J_y(x) = \int\limits_{P \in \mathcal{D}(x,t)} \left| \boldsymbol{e}_y \times \boldsymbol{p}_P \right|^2 da_P$$

is the *area moment of inertia* of the beam cross-section and

$$\tan\theta(x,t) = \frac{w'(x,t)}{1+u'(x,t)}$$

The *strain* is given by

$$\varepsilon(x,t) := l(x,t) - 1 = \sqrt{(1+u')^2 + (w')^2} - 1 = \sqrt{(1+2u' + (u')^2 + (w')^2} - 1$$

and the curvature by

$$\kappa = \frac{w'u'' - (1+u')w''}{((1+u')^2 + (w')^2)^{\frac{3}{2}}}$$

We thus have six unknowns. $u, w, \psi, T_x, T_y, M_y$ and six equations. Note that θ and ε may both be expressed in terms of u and w.

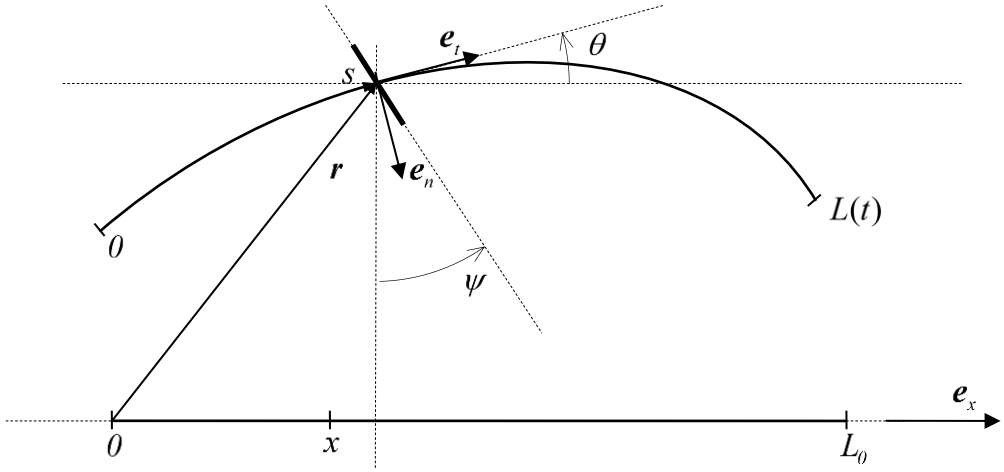

Figure A.6 Part of the beam centre line and the definition of sectional and external forces and moments

5.2 A.2 Linearized equations of motion

We assume that $|u'|, |w'| \ll 1$ and obtain the approximations

$$\tan\theta(x,t) \cong w'(x,t) \Leftrightarrow \theta(x,t) \cong w'(x,t)\,,\ \varepsilon = \sqrt{(1+2u'+(u')^2+(w')^2}\,-1 \cong u' \tag{A.11}$$

This gives

$$T_n(x,t) = \beta G \mathcal{A}(x)(\psi(x,t) - w'(x,t))\,,\ T_t(x,t) = E\mathcal{A}(x)u'(x,t)\,, \tag{A.12}$$
$$M_b(x,t) = -EJ_y(x)\psi'(x,t)$$

and then

$$\begin{cases} T_x = \dfrac{(1+u')T_t + w'T_n}{\sqrt{(1+u')^2+(w')^2}} \cong T_t \cong E\mathcal{A}u' \\ T_z = \dfrac{w'T_t - (1+u')T_n}{\sqrt{(1+u')^2+(w')^2}} \cong -T_n \cong \beta G\mathcal{A}(\psi - w') \\ M_y = M_b \cong -EJ_y\psi' \end{cases} \tag{A.13}$$

We thus have, according to (A.7) and (A.13),

$$\begin{cases} T_x' = E(\mathcal{A}u')' = \ddot{u}m \\ T_z' = -\beta G(\mathcal{A}(w'-\psi))' = \ddot{w}m \\ T_x w' - T_z(1+u') - E(J_y\psi')' = -I_y\ddot{\psi} \end{cases} \tag{A.14}$$

and then

$$\begin{cases} E(\mathcal{A}u')' = \ddot{u}m \\ \beta G(\mathcal{A}(w'-\psi))' = \ddot{w}m \\ E\mathcal{A}u'w' - \beta G\mathcal{A}(w'-\psi)(1+u') - E(J_y\psi')' = -I_y\ddot{\psi} \end{cases} \tag{A.15}$$

Now consider a beam with homogeneous and constant cross-section $I_y(x) = I_0$, $J_y(x) = J_0$, $\mathcal{A}(x) = A_0$ and $m(x) = m_0$. We also assume that the beam is subjected to an axial tension $T_x(x,t) = T \geq 0$ where T is a constant. From (A.15) it follows that

$$\begin{cases} EA_0u'' = \ddot{u}m_0 \\ \psi' = w'' - \dfrac{m_0}{\beta GA_0}\ddot{w} \\ EA_0(u'w')' - \beta GA_0(w'-\psi)'(1+u') - \beta GA_0(w'-\psi)u'' - EJ_0\psi''' = -I_0\ddot{\psi}' \end{cases} \tag{A.16}$$

It follows from $T = EA_0 u'(x,t)$ that

$$u'(x,t) = \frac{T}{EA_0} \Rightarrow u(x,t) = \frac{T}{EA_0} x + f(t)$$

Using the boundary condition it follows that $u(0,t) = 0 \Rightarrow f(t) = 0$ and this then implies $\dot{u} = 0,\ u'' = 0$. Note that in this case

$$\kappa = \frac{w'u'' - (1+u')w''}{((1+u')^2 + (w')^2)^{\frac{3}{2}}} \cong -w''$$

Compatibility with the linearization presumption requires that $T \ll EA_0$ and we then have

$$\begin{cases} \psi' = w'' - \dfrac{m_0}{\beta G A_0} \ddot{w} \\ Tw'' + \beta G A_0 (w' - \psi)' - EJ_0 \psi''' = -I_0 \ddot{\psi}' \end{cases} \qquad \text{(A.17)}$$

Using $(A.17)_1$ we obtain

$$\psi''' = w'''' - \frac{m_0}{\beta G A_0} \ddot{w}'',\ \ \ddot{\psi}' = \ddot{w}'' - \frac{m_0}{\beta G A_0} \ddot{w}''$$

This inserted into $(A.17)_2$ gives

$$Tw'' + \ddot{w} m_0 - EJ_0 (w'''' - \frac{m_0}{\beta G A_0} \ddot{w}'') = -I_0 (\ddot{w}'' - \frac{m_0}{\beta G A_0} \ddot{w}'')$$

and we then have the partial differential equation

$$w^{(4)} - (\frac{\rho_0}{\beta G} + \frac{I_0}{EJ_0}) \ddot{w}'' + \frac{m_0}{EJ_0} \ddot{w} - \frac{T}{EJ_0} w'' + \frac{I_0}{EJ_0} \frac{\rho_0}{\beta G} \ddot{w}'' = 0 \qquad \text{(A.18)}$$

Using the relations

$$\rho_0 = \frac{m_0}{A_0} = \frac{I_0}{J_0}$$

in (A.18) one obtains

$$w^{(4)} - \rho_0 (\frac{1}{\beta G} + \frac{1}{E}) \ddot{w}'' + \frac{m_0}{EJ_0} \ddot{w} - \frac{T}{EJ_0} w'' + \frac{\rho_0^2}{\beta G E} \ddot{w}'' = 0 \qquad \text{(A.19)}$$

In general the coefficients $\rho_0(\frac{1}{\beta G}+\frac{1}{E})$, $\frac{\rho_0^2}{\beta GE}$ are very small and we may neglect the corresponding terms and obtain the differential equation

$$w^{(4)}+\frac{m_0}{EJ_0}\ddot{w}-\frac{T}{EJ_0}w''=0 \tag{A.20}$$

After solving this for $w=w(x,t)$, with appropriate boundary and initial conditions, we may calculate the shear using the following equation

$$\psi'=w''-\frac{\rho_0}{\beta G}\ddot{w}\cong w'' \tag{A.21}$$

5.3 A.2 The beam with a sliding proof mass

Position vector of the proof mass $\boldsymbol{r}_P=\boldsymbol{r}_P(t)=\boldsymbol{e}_x x_P(t)+\boldsymbol{e}_z(W_0(t)+z_P(t))$ where $x=x_P(t)$, $z_P=z_P(t)$ are the coordinate for the proof mass and $\boldsymbol{W}(t)=\boldsymbol{e}_z W_0(t)$ is the motion of the beam support. See Figure A.7. Equations of motion for the proof mass

$$\begin{cases}\boldsymbol{N}+\boldsymbol{f}=\ddot{\boldsymbol{r}}_p m\\ M=I\ddot{\theta}\end{cases} \tag{A.22}$$

where $\ddot{\boldsymbol{r}}_p=\boldsymbol{e}_x\ddot{x}_P+\boldsymbol{e}_z(\ddot{W}_0+\ddot{z}_P)$, $\boldsymbol{N}$ and $\boldsymbol{f}$ are the normal force and the friction force on the proof mass from the beam, respectively, and M is the moment from the beam. The moment of inertia of the proof mass is denoted I and θ denotes the rotation angle of the proof mass, see Figure A.7 below! We have $\boldsymbol{N}=\boldsymbol{e}_n N$, $\boldsymbol{f}=\boldsymbol{e}_t f$ and

$$f=-\mu|N|\frac{\dot{x}_P}{|\dot{x}_P|},\ \dot{x}_P\neq 0,\ |f|\le -\mu|N|,\ \dot{x}_P=0 \tag{A.23}$$

We use the following notation

$$w(x,t)=\begin{cases}w^-(x,t),\ 0\le x<x_P(t)\\ w^+(x,t),\ x_P(t)\le x<L_0\end{cases}$$

where we assume that the functions w^- and w^+ are continuously differentiable with finite left and right limits, respectively of all its derivatives

at point $x = x_P(t)$. We have the constraint equations

$$z_P(t) = w^-(x_P(t),t) = w^+(x_P(t),t)$$

reflecting the continuity of the beam.

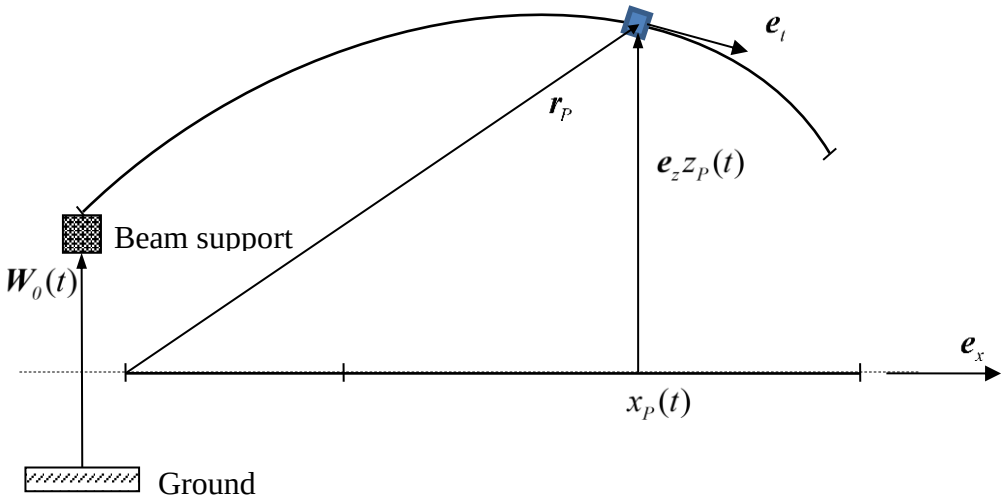

Figure A.7 Part of the beam centre line and the definition of sectional and external forces and moments

The velocity of the proof mass is then given by

$$\dot{\boldsymbol{r}}_P(t) = \boldsymbol{e}_x \dot{x}_P(t) + \boldsymbol{e}_z(\dot{W}_0(t) + w^{-\prime}(x_P(t),t))\dot{x}_P(t) + \dot{w}^-(x_P(t),t))) =$$

$$\boldsymbol{e}_x \dot{x}_P(t) + \boldsymbol{e}_z(\dot{W}_0(t) + w^{+\prime}(x_P(t),t))\dot{x}_P(t) + \dot{w}^+(x_P(t),t)))$$

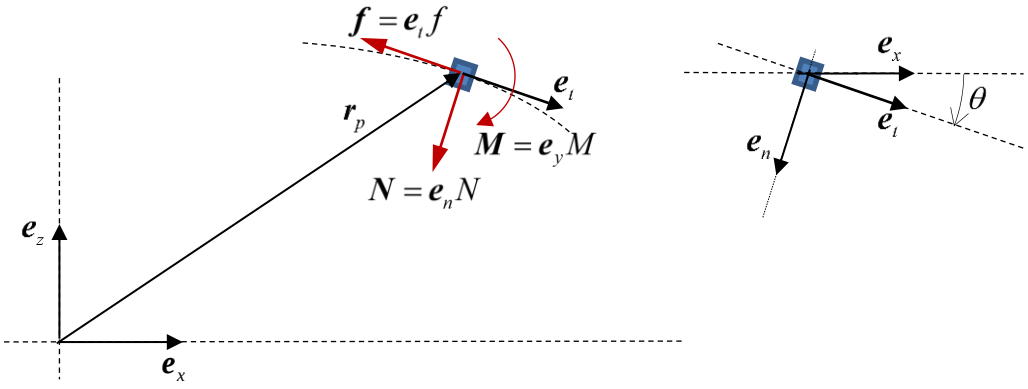

Figure A.8 Part of the beam centre line and the definition of sectional and

external forces and moments

and the acceleration by

$$\ddot{\boldsymbol{r}}(t) = \boldsymbol{e}_x \ddot{x}_P(t) + \boldsymbol{e}_z (\ddot{W}_0(t) + w^{-\prime\prime}(x_P(t),t)\dot{x}_P(t)^2 + \dot{w}^{-\prime}(x_P(t),t)\dot{x}_P(t) +$$

$$w^{-\prime}(x_P(t),t)\ddot{x}_P(t) + \dot{w}^{-\prime}(x_P(t),t))\dot{x}_P(t) + \ddot{w}^{-}(x_P(t),t)) = \boldsymbol{e}_x \ddot{x}_P(t) + \boldsymbol{e}_z (\ddot{W}_0(t) +$$

$$w^{-\prime\prime}(x_P(t),t)\dot{x}_P(t)^2 + 2\dot{w}^{-\prime}(x_P(t),t)\dot{x}_P(t) + w^{-\prime}(x_P(t),t)\ddot{x}_P(t) + \ddot{w}^{-}(x_P(t),t)) =$$

$$\boldsymbol{e}_x \ddot{x}_P(t) + \boldsymbol{e}_z (\ddot{W}_0(t) + w^{+\prime\prime}(x_P(t),t)\dot{x}_P(t)^2 + 2\dot{w}^{+\prime}(x_P(t),t)\dot{x}_P(t) +$$

$$w^{+\prime}(x_P(t),t)\ddot{x}_P(t) + \ddot{w}^{+}(x_P(t),t)) \qquad \text{(A.24)}$$

We have, see Figure A.8,

$$\boldsymbol{e}_y \sin\theta = \boldsymbol{e}_x \times \boldsymbol{e}_t = \boldsymbol{e}_x \times \frac{\boldsymbol{e}_x(1+u^{-\prime}) + \boldsymbol{e}_z w^{-\prime}}{\sqrt{(1+u^{-\prime})^2 + (w^{-\prime})^2}} = \frac{\boldsymbol{e}_y(-w^{-\prime})}{\sqrt{(1+u^{-\prime})^2 + (w^{-\prime})^2}}$$

$$\boldsymbol{e}_y \sin\theta = \boldsymbol{e}_x \times \boldsymbol{e}_t = \boldsymbol{e}_x \times \frac{\boldsymbol{e}_x(1+u^{+\prime}) + \boldsymbol{e}_z w^{+\prime}}{\sqrt{(1+u^{+\prime})^2 + (w^{+\prime})^2}} = \frac{\boldsymbol{e}_y(-w^{+\prime})}{\sqrt{(1+u^{+\prime})^2 + (w^{+\prime})^2}}$$

Thus, if $\boldsymbol{e}_t = \boldsymbol{e}_t(x,t)$ is continuous at $x = x_P(t)$ then we may conclude that

$$\sin\theta = \frac{-w^{-\prime}}{\sqrt{(1+u^{-\prime})^2 + (w^{-\prime})^2}} = \frac{-w^{+\prime}}{\sqrt{(1+u^{+\prime})^2 + (w^{+\prime})^2}} \qquad \text{(A.25)}$$

Equations of motion for the beam segment supporting the proof mass, neglecting the inertia of the beam segment, see Figure A.9,

$$\begin{cases} T_t^- - T_t^+ + f = 0 \\ T_n^- - T_n^+ + N = 0 \\ M_b^- - M_b^+ - M = 0 \end{cases} \qquad \text{(A.26)}$$

We then have

$$\begin{cases} EA_0(\varepsilon^{-\prime} - \varepsilon^{+\prime}) + f = 0 \\ \beta G A_0(\psi^- - \psi^+) + N = 0 \\ EJ_0(\psi^+ - \psi^-) - M = 0 \end{cases} \tag{A.27}$$

where we have used (A.21). The equations of motion for the proof mass are given by (A.22) or

$$\begin{cases} N_x + f_x = \ddot{x}_p m \\ N_z + f_z = \ddot{z}_P m \\ M = I\ddot{\theta} \end{cases} \tag{A.28}$$

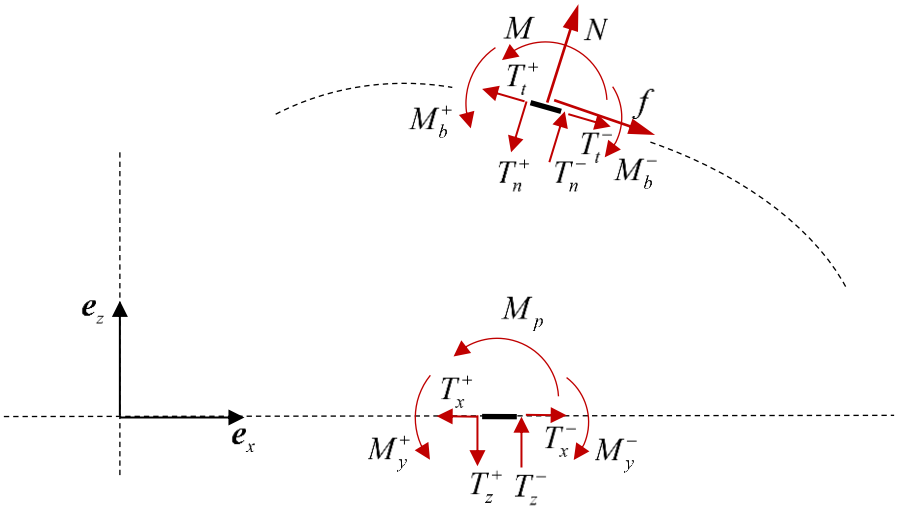

Figure A.9 Part of the beam centre line and the definition of sectional and external forces and moments

We have the relations

$$\boldsymbol{N} = \boldsymbol{e}_x N_x + \boldsymbol{e}_z N_z = \boldsymbol{e}_n N = \frac{\boldsymbol{e}_x w' N + \boldsymbol{e}_z(-(1+u'))N}{\sqrt{(1+u')^2 + (w')^2}}$$

$$\boldsymbol{f} = \boldsymbol{e}_x f_x + \boldsymbol{e}_z f_z = \boldsymbol{e}_t f = \frac{\boldsymbol{e}_x f(1+u') + \boldsymbol{e}_z f w'}{\sqrt{(1+u')^2 + (w')^2}}$$

from which it follows that

$$\begin{cases} N_x = \dfrac{w'N}{\sqrt{(1+u')^2+(w')^2}}, & N_z = \dfrac{-(1+u')N}{\sqrt{(1+u')^2+(w')^2}} \\ f_x = \dfrac{f(1+u')}{\sqrt{(1+u')^2+(w')^2}}, & f_z = \dfrac{fw'}{\sqrt{(1+u')^2+(w')^2}} \end{cases} \tag{A.29}$$

Assuming $|u'|,|w'| \ll 1$ one obtains the approximations

$$\theta(t) \cong -w^{-\prime}(x_P(t),t) = -w^{+\prime}(x_P(t),t)$$

$$\dot{\theta}(t) \cong -(w^{-\prime\prime}(x_P(t),t)\dot{x}_P(t) + \dot{w}^{-\prime}(x_P(t),t)) = -(w^{+\prime\prime}(x_P(t),t)\dot{x}_P(t) + \dot{w}^{+\prime}(x_P(t),t))$$

$$\ddot{\theta}(t) \cong -(w^{-\prime\prime\prime}(x_P(t),t)\dot{x}_P(t)^2 + w^{-\prime\prime}(x_P(t),t)\ddot{x}_P(t) + 2\dot{w}^{-\prime\prime}(x_P(t),t)\dot{x}_P(t) +$$

$$\ddot{w}^{-\prime}(x_P(t),t)) = -(w^{+\prime\prime\prime}(x_P(t),t)\dot{x}_P(t)^2 + w^{+\prime\prime}(x_P(t),t)\ddot{x}_P(t) + 2\dot{w}^{+\prime\prime}(x_P(t),t)\dot{x}_P(t) +$$

$$\ddot{w}^{+\prime}(x_P(t),t)) \tag{A.30}$$

from which it follows that

$$\begin{cases} N_x = \dfrac{w'N}{\sqrt{(1+u')^2+(w')^2}} \cong w'N, & N_z = \dfrac{-(1+u')N}{\sqrt{(1+u')^2+(w')^2}} \cong -N \\ f_x = \dfrac{f(1+u')}{\sqrt{(1+u')^2+(w')^2}} \cong f, & f_z = \dfrac{fw'}{\sqrt{(1+u')^2+(w')^2}} \cong fw' \end{cases} \tag{A.31}$$

Inserting (A.31) into (A.28) gives

$$\begin{cases} w'N + f = \ddot{x}_P m \\ fw'(x_P,t) - N = (\ddot{W}_0 + w''(x_P,t)\dot{x}_P{}^2 + 2\dot{w}'(x_P,t)\dot{x}_P + w'(x_P,t)\ddot{x}_P + \ddot{w}(x_P,t))m \\ M = -I(w'''(x_P,t)\dot{x}_P^2 + w''(x_P,t)\ddot{x}_P + 2\dot{w}''(x_P,t)\dot{x}_P + \ddot{w}'(x_P,t)) \end{cases} \tag{A.32}$$

where w here represents w^- or w^+.

$$N(t) = f(t)w'(x_P,t) - (\ddot{W}_0 + w''(x_P,t)\dot{x}_P{}^2 + 2\dot{w}'(x_P,t)\dot{x}_P + w'(x_P,t)\ddot{x}_P + \ddot{w}(x_P,t))m \tag{A.33}$$

$$f(t) = \ddot{x}_P(t)m - w'(x_P,t)N(t)$$

Elimination of N gives

$$w'(x_P,t)(f(t)w'(x_P,t)-(\ddot{W}_0+w''(x_P,t)\dot{x}_P{}^2+2\dot{w}'(x_P,t)\dot{x}_P+w'(x_P,t)\ddot{x}_P+$$

$$\ddot{w}(x_P,t))m+f(t)=\ddot{x}_P(t)m$$

and by re-arranging one obtains

$$-w'(x_P,t)(\ddot{W}_0+w''(x_P,t))\dot{x}_P{}^2+2\dot{w}'(x_P,t))\dot{x}_P+\ddot{w}(x_P,t))m+(1+(w'(x_P,t))^2)f(t)=$$

$$(1+(w'(x_P,t))^2)\ddot{x}_P(t)m$$

which, since $|w'|\ll 1$, is approximately equal to

$$-w'(x_P,t)(\ddot{W}_0+w''(x_P,t))\dot{x}_P{}^2+2\dot{w}'(x_P,t))\dot{x}_P+\ddot{w}(x_P,t))m+f(t)=\ddot{x}_P(t)m \quad \text{(A.34)}$$